Combined Gleeble physical welding simulation and low-cycle thermo-mechanical fatigue for heat-affected zone material for 9Cr steel: Experimental testing and through-process model

Combined Gleeble physical welding simulation and low-cycle thermo-mechanical fatigue for heat-affected zone material for 9Cr steel: experimental testing and through-process model

P. Mac Ardghail[1,2], R.A. Barrett[1,2,3], N. Harrison[1,2,3], I. Sabirov[4,5], J. Llorca[4,5], S. B. Leen[1,2,3]

[1]Mechanical Engineering, University of Galway, Ireland.

[2]Ryan Institute for Marine, Energy and Environment, University of Galway, Ireland.

[3]I-Form Advanced Manufacturing Research Centre, Ireland.

[4] Institute IMDEA Materials, C/Eric Kandel 2, 28906 Getafe, Madrid, Spain

[5] Department of Materials Science, Technical University of Madrid, E.T.S. de Ingenieros de Caminos, 28040 Madrid, Spain

(sean.leen@universityofgalway.ie)

Abstract

There is an urgent need to operate thermal power plant at significantly higher temperatures, pressures and flexibility, in order to reduce emissions, increase efficiency and facilitate uptake of renewable energy. This demands significantly improved design of welded connections for thermo-mechanical fatigue (TMF). A common mode of high temperature failure for welded 9Cr steels in such plant is Type IV failure, due to reduced hardness in the inter-critical heat affected zone (IC-HAZ). Little or no work has been previously conducted on TMF characterisation of HAZ of 9Cr steels. This work presents development of a combined Gleeble physically-simulated welding process for P91 heat affected zone, based on measured thermal histories from bead-on-plate welding trials, with in-situ low cycle thermo-mechanical fatigue up to 650^{o}C. The simulated welding process, including post-weld heat treatment (PWHT), is shown to have significant effect on both microstructure and TMF behaviour, including life. The as-welded condition is shown to have the cyclically hardest stable response and the longest life, whereas the PWHT and parent material (PM) cases have similar cyclically soft responses and lives. A recently-developed through-process, physically-based, thermal-metallurgical-

mechanical model is adapted and applied to the simulated welding thermal cycle and TMF testing for PM and HAZ specimens. The model is calibrated and validated against high temperature low-cycle fatigue and low-cycle TMF data for PM in the range 400°C to 600°C, for different strain-ranges and strain-rates. It is also shown to capture some observed general trends for the simulated HAZ-TMF testing, especially the significant softening effect of PWHT and the significant increase in cyclic strength for the as-welded condition.

1. Introduction

Thermal power plant has traditionally operated under 'base-load' conditions, where power output, and therefore mechanical loading, was near-constant throughout the life of the power plant. However, modern plant operating conditions are increasingly required to operate under flexible operating conditions to facilitate increased reliance on renewable energy sources, which produce variable amounts of power during the day, and due to improved monitoring of the power grid, allowing plant output to be adjusted to suit demand, which varies during the day. Flexible operation leads to increased cyclic variations in plant steam pressure and temperature, thereby subjecting plant material to cyclic loading. Furthermore, there is an impetus to operate plant at ever-increasing temperatures, in order to increase efficiency and reduce emissions. Hence, there is significant interest in development of materials for higher temperature, as well as assessment of the higher temperature capabilities of current power plant materials.

Among the power plant materials in use are the 9Cr family of steels. These steels owe their strength to high-dislocation-density martensitic microstructures with nano-precipitate strengthening [1] but this microstructure is known to degrade under cyclic loading conditions [2]. As the microstructure degrades, the strength reduces and the service life of 9Cr power plant

components is reduced. In welded connections, the welding process disrupts the 9Cr steel microstructure and therefore the integrity of the steel even before it is degraded under cyclic loading conditions. The worst-affected region tends to be the inter-critical heat-affected zone (ICHAZ) of welded joints [3-5], a region adjacent to the parent metal (PM). A common mode of high temperature failure for welded 9Cr steels in such plant is Type IV failure, due to reduced hardness in the inter-critical heat affected zone (IC-HAZ). Little or no work has been previously conducted on TMF characterisation of HAZ of 9Cr steels.

TMF testing is an important method to assess plant materials for flexible operation. In this work, a programme of Gleeble physical simulation of welding, combined with in-situ thermo-mechanical fatigue testing. TMF testing is conducted on the parent metal and the simulated HAZ material, with and without post-weld heat treatment, in-situ in the Gleeble. The focus of this work is an assessment of the relative performance of HAZ, both with and without PWHT, compared to parent P91 material, specifically in terms of maximum and minimum stress cyclic response and numbers of cycles to failure, viz. TMF life. Furthermore, an enhanced version of a recently-developed physically-based, through-process thermal-metallurgical-mechanical model, which simulates both the welding process, specifically the associated microstructure evolution, and subsequent thermo-mechanical behaviour, is presented for comparison with the Gleeble combined welding-TMF test data, in terms of maximum and minimum stress cyclic response [6]. The model is initially compared with high temperature low cycle fatigue (HTLCF) and TMF test data for P91 parent metal from a previous test program. A key novelty here is the application of this model to P91 HAZ and to the TMF-IP and –OP test conditions, which are particularly relevant to current unexpected high flexibility power plant high temperature transients, e.g. above 600 ^{o}C, and future high efficiency, high flexibility operating conditions, up to or above 600 ^{o}C.

2. Experimental Methodology

The simulated welding tests were conducted on a Gleeble 3800. A more complete description of the Gleeble 3800 test rig is given by Bíró and Csizmadia [7], including examples of its application; further applications are presented by Castro Cerda et al. [8] and Rahimian et al. [9]. For brevity, a Gleeble 3800 is capable of simulated welding temperatures (up to 3,000^{o}C) with high heating rates (up to 10,000^{o}C/s) and cooling rates (-10,000^{o}C/s) in electrically-conductive materials. Heating and high heating rates are achieved by electrical resistance heating, in which electric current is passed though the test specimen. High cooling-rates are achieved using cooling jets and high thermal conductivity grips, which allow the rapid dissipation of heat, to hold the specimen. The Gleeble 3800 is also capable of tensile and cyclic loading (20 metric tonnes in compression, 10 metric tonnes in tension) at a range of strain-rates (crosshead speed from 0.001 mm/s to 2,000 mm/s) [10], making it suitable for TMF testing. The purpose of the present simulated welding trials was to generate P91 ICHAZ material and use this for TMF testing. The test specimens were machined from P91 pipe material (UNS K91560, ASTM A335 Grade P91) to the specifications described in Figure 2. The P91 material used here is an ex-service sample. The material, provided by ESB Energy International, was subjected to 35,168 hrs of service under subcritical loading conditions. The material was removed from service for operational reasons and was only subjected to operation at temperatures below 485 °C (normal operating conditions for Lough Ree power station is in the 460 to 485 °C temperature range). Table 1 provides a comparison of the chemical composition of the ex-service P91 (ES-P91) compared to as-received P91 (AR-P91). Apart from simulated as-welded (AW) ICHAZ specimens, tests on PM and simulated ICHAZ with PWHT were conducted. This facilitates a comparison of the PM, ICHAZ (AW) and ICHAZ (PWHT) TMF

behaviour, allowing for investigation of the effect of both welding and PWHT separately. The test matrix for the TMF testing is displayed in Table 2.

Table 1: Chemical composition of P91 steels in wt%. ES-P91 (as used here) and AR-P91 steels denote 'ex-service' and 'as-received' respectively. The balance is made up of Fe.

	Al	C	Cr	Mn	Mo	N	Nb	Ni	P	S	Si	V	W
ES-P91	0.007	0.10	8.48	0.42	0.94	0.058	0.07	0.19	0.013	-	0.26	0.204	-
AR-P91	0.007	0.12	8.60	-	1.02	0.06	0.07	-	0.017	<0.002	0.34	0.24	0.03

Table 2. TMF test matrix for P91 for all specimens, for both TMF-IP and TMF-OP.

Test condition	Value
ε-rate	0.04 %/s
ε-range	+0.4%, -0.4%
Wave *t*	40 s
T-range	520°C to 650°C

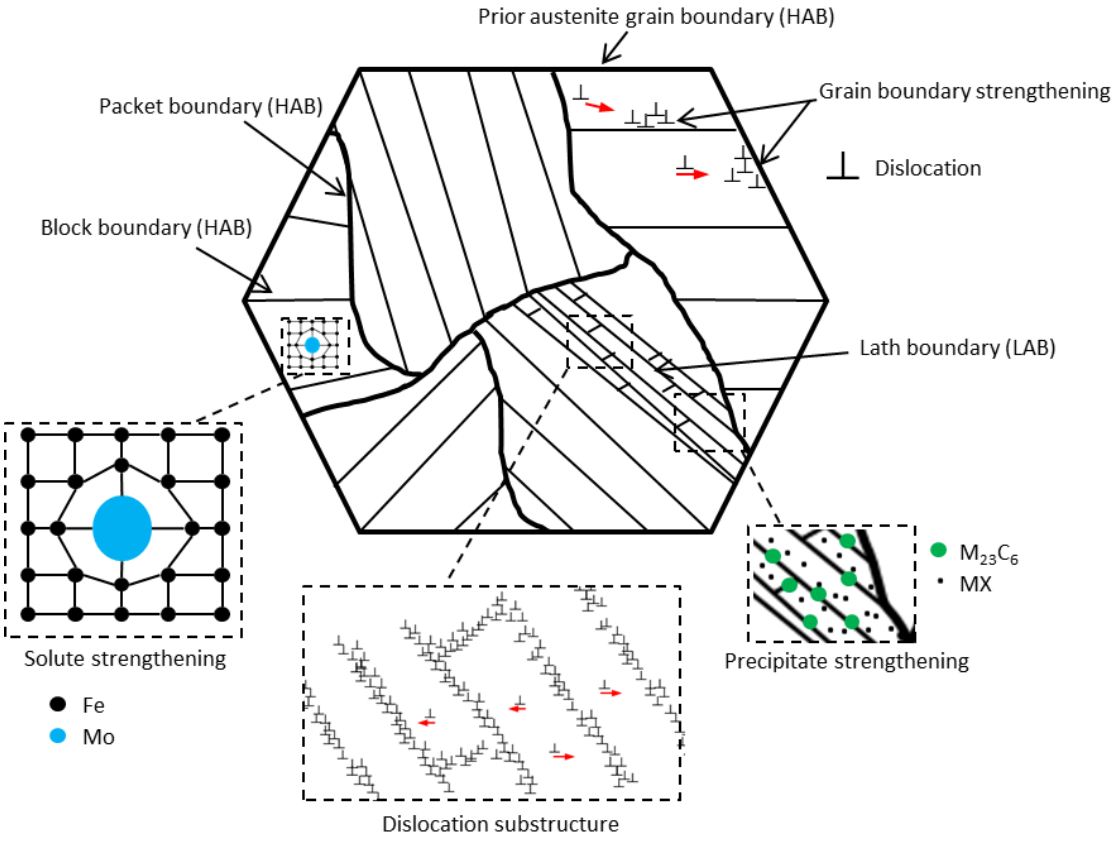

Figure. 1. Schematic depiction of hierarchical microstructure of 9Cr steels and strengthening features of microstructure. Figure following Barrett et al. [11].

9Cr steels achieve high temperature strength via a complex hierarchical microstructure as shown in Fig. 1. Dislocations are primarily located in laths, at the lowest microstructure level. The angle between two adjacent laths is typically less than 5^{o} [12, 13]. Such 'low-angle' boundaries (LAB) do not present significant obstacles to dislocation motion. Laths are organised into blocks and blocks into packets, within the boundaries of prior-austenite grains (PAG) [12]. PAG are typically 10 μm to 60 μm in size [14, 15, 16]. The mismatch-angle between blocks, packets and grains are greater than 10 to 15^{o} [17] and are defined as 'high-angle' boundaries (HAB), which do retard dislocation motion. Figure 3 shows the typical measured effect of temperature on the some key tensile properties of P91. Appendix 1 shows sample high temperature low cycle fatigue test results, across a range of temperatures from 20 ^{o}C to 600 ^{o}C, for ES-P91 material at University of Galway, from the work of Farragher [18].

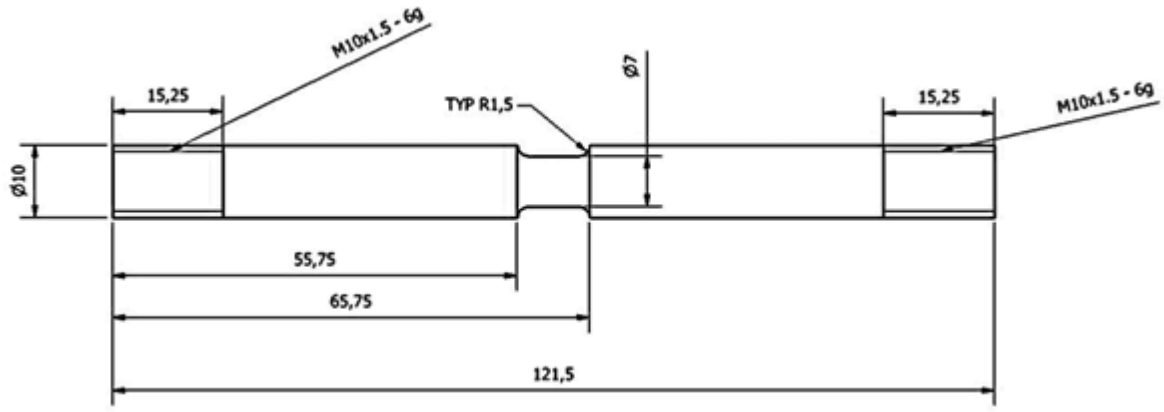

Figure 2. Specifications of the test specimens used for simulated welding and TMF testing. Dimensions in mm.

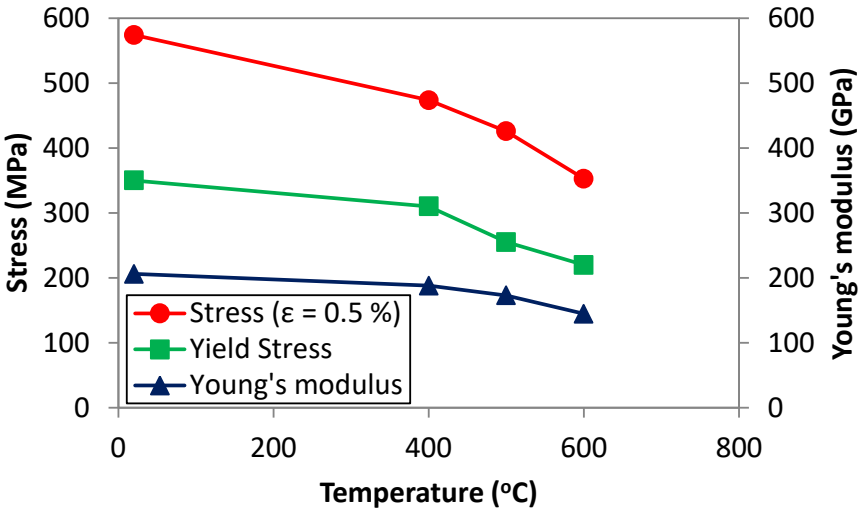

Figure 3. Temperature dependence of yield stress and Young's modulus in ES-P91 steel [11].

Table 3. Austentic-martensitic phase transformation temperatures.

A_{c1}	A_{c3}	M_s	M_f
830°C [19]	920°C [19]	400°C [20]	100°C [20]

Three materials were tested: PM, simulated as-welded ICHAZ and simulated ICHAZ with PWHT. For PWHT conditions, a peak temperature of 760°C, a hold time of 30 minutes and heating and cooling rates of 220°C/hour were selected. These PWHT conditions are consistent with the PWHT standard ISO/TR 14745:2015 [21]. The maximum operating temperature of P91 steel is generally considered to be between about 600°C and 650°C. On the one hand, the present work is focussed on evaluating the performance of welded connections at higher temperatures, with a view to reduced emissions, e.g. via ultra-super critical operation. On the other hand, recent plant experience indicates the more frequent occurrence of over-heating 'trips', with significant excursions, e.g. up to 650°C, above operating temperatures of up to 500 °C, associated with increasing high flexibility plant operation, e.g. for complementarity with renewable sources. Hence, the maximum temperature in the TMF cycles was defined to be 650°C, and the minimum temperature at 520°C, with a cycle time defined as 40 seconds, based on a recently-observed overheating 'trip' event in power plant operation in Ireland [22]. The

selected strain-range of 0.8% and strain-rate (0.04 %/s) are also typical representative values used in TMF testing of 9Cr and similar steels, and are typical of plant operational conditions, e.g. see Farragher et al. [23].

The choice of test conditions in the test matrix was also influenced by certain pragmatic considerations. Specifically, it was required to ensure specimen failure within 8 hours of testing, based on previous experience with control thermocouples detaching after about 8 hours. Hence, a relatively rapid strain-rate was used to achieve a sufficient number of cycles within the 8-hour period. The maximum temperature of 650^{o}C was chosen because (a) it is an ultra-supercritical operating temperature, (b) this is at the limit of the operating range for 9Cr steel and is therefore of interest for power plants moving to increased efficiency and (c) previous other work has already examined the effects of lower temperature ranges, e.g. 400^{o}C to 600^{o}C [24], including high temperature low cycle fatigue of cross-weld specimens, as well as weld metal and parent metal P91 specimens e.g. see Farragher et al. [4].

Before the testing campaign, the hot zone transducer (HZT) extensometer of the Gleeble, manufactured by Dynamic Systems Inc., was used to control the plastic strain. A direct correlation between the plastic strain measurements obtained from the HZT extensometer and those from the machine was established. However, use of the HZT extensometer during the experiment had to be discontinued since it was found that the extensometer was heated by heat radiation from the hot sample, causing the springs fixing the extensometer to the gauge length to weaken, resulting in the slippage of the extensometer pins on the surface of the gauge length. Therefore, it was decided to control the plastic strain using the machine instead.

A schematic representation of the in-phase (IP) and out-of-phase (OP) TMF loading cycles is shown in Fig. 4. For IP testing, the maximum tensile strain is synchronised with the peak temperature and the maximum compressive strain with the minimum temperature. For the OP test, the maximum tensile and compressive strains are synchronised with the minimum and maximum temperatures, respectively. These loading cycles are typical for TMF testing. Since the primary focus of attention in this work is on the Gleeble simulation of HAZ conditions, only one representative strain range is studied. Future work will investigate a broader range of strain-ranges.

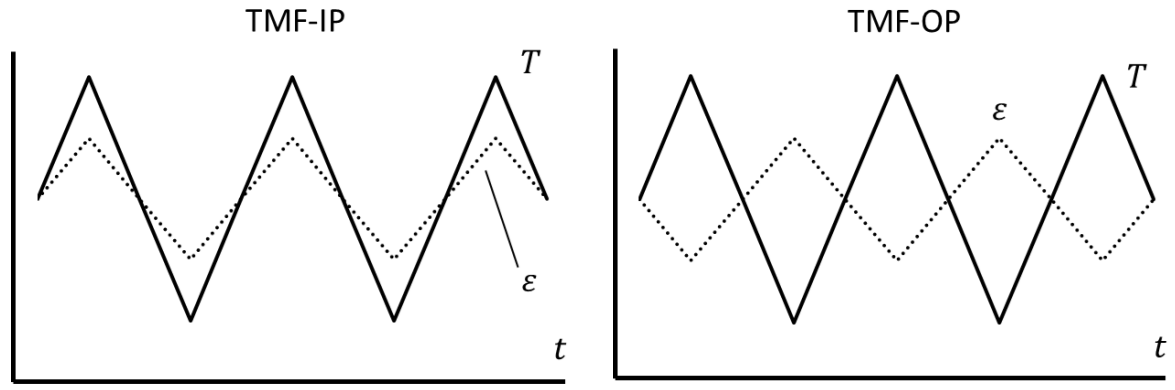

(a) (b)

Fig. 4. A schematic representation of (a) TMF-IP and (b) TMF-OP temperature, T, and strain, ε, histories. Note that ε refers to mechanical strain.

The physical welding simulation temperature cycle applied to the test specimens to generate simulated ICHAZ material is shown in Fig. 5a, including the A_{c1} and A_{c3}, start and end temperatures for austenite transformation. Figure 5b show a section view of a typical HAZ Gleeble test specimen.

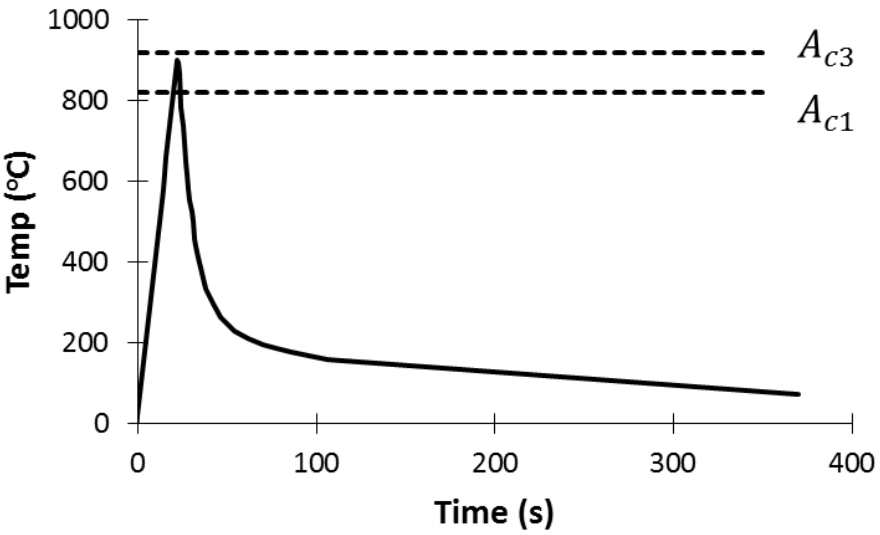

(a)

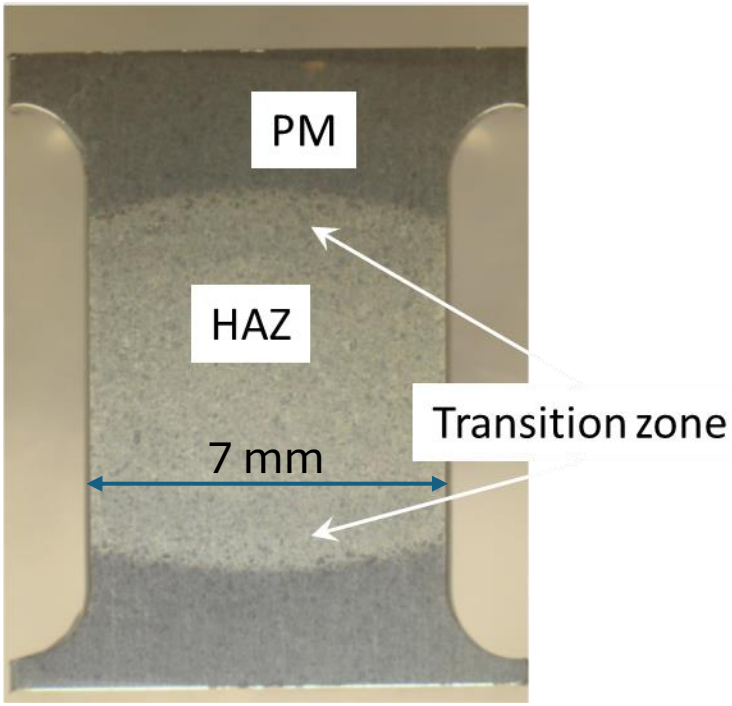

(b)

Fig. 5. (a) The defined temperature-time curve, extrapolated from a finite element modelling of bead-on-plate welding trials for P91 [25] predicted curve, for Gleeble simulation of ICHAZ, and (b) the cross-section of typical HAZ specimen showing HAZ, PM and transition zones. For scale, the HAZ section is 7 mm wide.

3. Thermal-metallurgical-mechanical model for welding and TMF

We adapt a process-structure-property model from the our previous work [6], which consists of (i) a solid state phase transformation model, including phase transformation from tempered and untempered martensite and austenite, (ii) a microstructure evolution model, incorporating effects of thermal cycle on prior austenite grain (PAG) size (recrystallization and grain growth), hardness, lath width, $M_{23}C_6$ precipitate volume fraction and diameter, and (iii) a physically-based (dislocation mechanics) unified viscoplasticity constitutive model, using rule of mixtures for combination of martensite-austenite phases. The latter model incorporates effects of PAG size, lath width, precipitate-dependent yield stress and precipitate coarsening effects, within a dislocation mechanics kinematic hardening framework, with Kocks-Mecking type accumulation-annihilation, and dislocation-based isotropic softening effects. The thermal-metallurgical model was calibrated against published heat treatment microstructure data for P91 steels, across a range of temperatures, for PAG size (recrystallization and grain growth), hardness evolution with time at various normalising and PWHT temperatures, lath width relationship with hardness, temperature and PAG size, and $M_{23}C_6$ precipitate volume fraction and diameter temperature-time dependency; see [6], for example, for further details on this aspect.

The physically-based, constitutive model implemented here is based on dislocation mechanics theory and incorporates both isotropic softening and kinematic hardening, using Taylor type formulations in both cases. Key inputs to this model include the results from the microstructure-evolution model, specifically, the volume-fractions of solid-state phases (tempered and newly-formed martensite, austenite), PAG size, lath-width and $M_{23}C_6$ precipitate diameter and area-fraction, as described below.

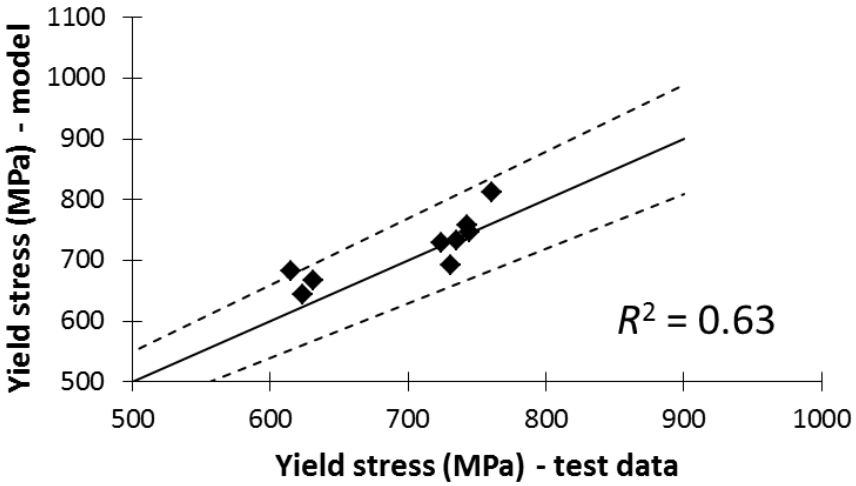

Fig. 6. A comparison between predicted yield stress and test data [15] at room-temperature. The dotted lines represent deviations of 10% from a perfect match.

The rate of equivalent plastic strain $\dot{p}$ is described using a hyperbolic sine flow rule, as follows:

$$\dot{p} = \alpha \sinh(\beta f) \tag{1}$$

where α and β are visco-plastic parameters, identified from monotonic data for 9Cr steel following the method described previously [6]. A constant value for β is identified while α is defined as proportional to the PAG size, *d*, as follows:

$$\alpha = n_3 d \tag{2}$$

where n_3 is a constant. The parameters for the hyperbolic sine flow rule are displayed in Table 6. The yield function *f* is defined as:

$$f = \sqrt{\frac{3}{2}(\boldsymbol{\sigma}' - \boldsymbol{\chi}'):(\boldsymbol{\sigma}' - \boldsymbol{\chi}')} + R - k_y \tag{3}$$

where $\boldsymbol{\sigma}'$ is the deviatoric stress tensor, $\boldsymbol{\chi}'$ is the deviatoric kinematic back-stress tensor, and ':' represents the scalar product of two tensors. *R* is an isotropic softening variable, representing the change (decrease) in size of the yield surface. The room-temperature yield stress for martensite (tempered or untempered), σ_y^0, is defined to be a function of the precipitate-diameter and precipitate area-fraction:

$$\sigma_y^0 = Q_1 e^{q_2 \theta} \tag{4}$$

where

$$Q_1 = Q_3 + Q_4 A_\theta \tag{5}$$

and Q_2, Q_3 and Q_4 are constants, with A_θ, the area fraction of precipitates, defined elsewhere [6, 25]. A temperature-dependent cyclic yield stress, k_y, is defined as:

$$k_y = \sigma_y^0 + Q_5 T + Q_6 \sigma_y^0 T \tag{6}$$

where T is temperature and Q_5, Q_6 are constants; the identified set of parameters for the yield stress model are given by MacArdghail et al. [6] and in Table 5. Fig. 6 shows a comparison of the model predicted yield stress values against test data for a range of different heat treatment conditions [6].

Table 5. Parameters of the unified visco-plasticity constitutive model using combined kinematic-isotropic hardening-softening, and damage and yield-stress evolution models [6].

Parameter	Value	Parameter	Value
a	0.33	n_6	0.023 K^{-1}
M	3	a_7	0.14
b	0.248 nm	Q_2	-0.0022 nm^{-1}
ρ_0	4.4×10^8 mm^{-2}	Q_3	1176 MPa
β	0.011 MPa^{-1}	Q_4	-72.73 MPa $\%^{-1}$
n_3	3.7×10^{-7} μm^{-1}	Q_5	-0.0773 MPa K^{-1}
n_4	0.0005	Q_6	-0.00117 K^{-1}
n_5	4.91×10^{-7}	Q_t	100 MPa

The kinematic back-stress tensor takes the form of a Taylor-type hardening:

$$\boldsymbol{\chi} = \left(aMGb\sqrt{\rho}\right)\boldsymbol{n} \tag{7}$$

where a is a constant, M is the Taylor factor, G is shear modulus, b is magnitude of the Burgers vector, ρ is dislocation-density and $\boldsymbol{n}$ is the tensor normal to the yield surface. Dislocation-density evolution is described as:

$$\dot{\rho} = \frac{\rho_0 \dot{\bar{\rho}}}{(1-\bar{\rho})^2} \tag{8}$$

where ρ_0 is initial dislocation density, identified from equation $\sigma_y = aMGb\sqrt{\rho_0}$. The identified value sits within the range of measured or previously published values, ranging from 7.9×10^7 mm^{-2} [26] to 9×10^8 mm^{-2} [1]. $\bar{\rho}$ is normalised dislocation-density:

$$\bar{\rho} = 1 - \frac{\rho_0}{\rho} \tag{9}$$

which evolves during plastic deformation, as follows:

$$\dot{\bar{\rho}} = g_1(\bar{\rho}_L - \bar{\rho})|\dot{p}| \tag{10}$$

where g_1 and $\bar{\rho}_L$ are both dependent on temperature and phase. In the martensite (tempered or newly-formed) phase, these are defined using double-sigmoidal equations (see [6] for detail) to represent temperature-dependency.

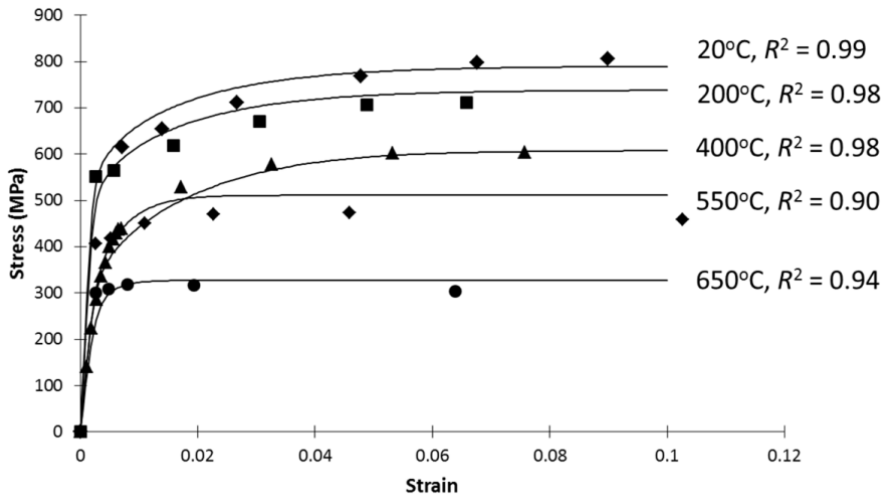

(a)

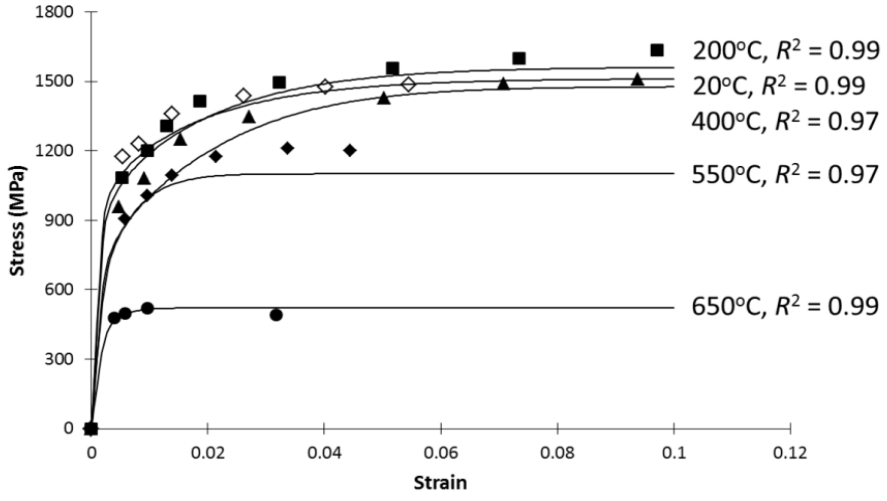

(b)

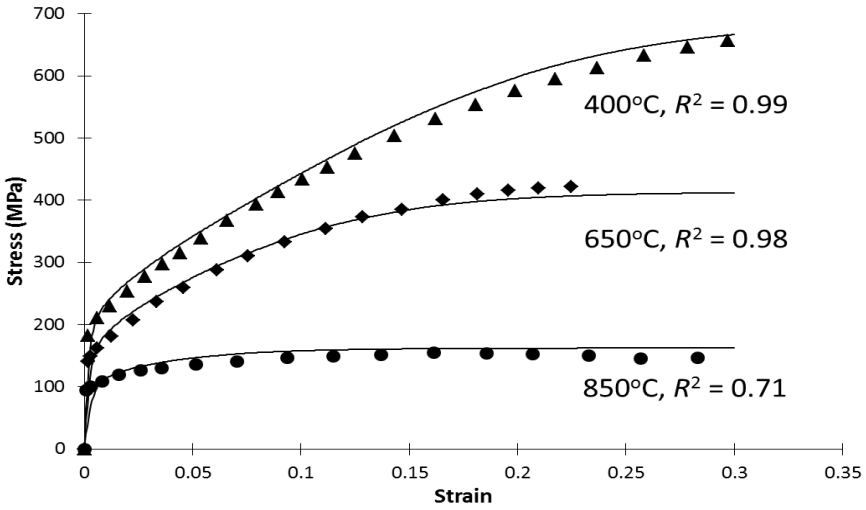

(c)

Fig. 7. Calibration of material model (lines) against test data [19] (points) for (a) tempered martensite, (b) untempered martensite and (c) austenite P92 across a range of temperatures.

The kinematic back-stress was calibrated against tensile test data from Yaghi et al. [19] across a range of temperatures for the three material phases (tempered and newly-formed martensite and austenite), as shown in Fig. 7. For mixed-phase material, e.g. when the material has partially transformed to austenite from martensite, a rule-of-mixtures approach is used to determine the values of g_1 and $\bar{\rho}_L$.

The isotropic softening model is intended to represent dislocations moving from within microstructure regions such as PAGs, packets or blocks to the boundaries, where annihilation occurs during kinematic hardening. It is assumed that annihilation of dislocations also occurs at boundaries, e.g. due to higher local dislocation-density and consequent reduction of distance between dislocations until they are within annihilation-distance, thus reducing overall dislocation-density and softening the material. The isotropic hardening variable R is defined as follows:

$$R = \alpha_g MGb\sqrt{\rho_{cyc}} \tag{11}$$

based on a 'cyclic' value of dislocation density, with evolution of ρ_{cyc} defined via:

$$\Delta\rho_{cyc} = \frac{\rho_0 \Delta\bar{\rho}_{cyc}}{\left(1 - \bar{\rho}_{cyc}\right)^2} \tag{12}$$

and the normalised value is:

$$\bar{\rho}_{cyc} = 1 - \frac{\rho_0}{\rho_{cyc}} \tag{13}$$

The normalised, cyclic dislocation-density evolution is based on the accumulated normalised dislocation-density within one half-cycle of plasticity:

$$\Delta\bar{\rho}_{cyc} = g_{1c}\left(\bar{\rho}_{Lc} - \bar{\rho}_{cyc}\right)\Delta\bar{\rho} \tag{14}$$

where

$$g_{1c} = n_4 g_1 \tag{15}$$

with g_1 defined in the Appendix and

$$\bar{\rho}_{Lc} = n_5 \bar{\rho}_L e^{n_6 T} \tag{16}$$

with n_4, n_5 and n_6 as constants (see Table 5). The model was calibrated against cyclic test data for parent metal P91 at a range of strain-ranges and temperatures (400 to 600°C), as shown in Fig. 8, thus demonstrating the ability of the model to represent HTLCF test data, including cyclic softening effects, for P91 PM. Figure 9 shows validation of the model for HTLCF conditions of 600°C, strain-rate 0.1%/s and strain-range 1%. It is seen here that the model captures the general trend and stabilised cycles very well but slightly underpredicts the 1st cycle maximum tensile and compressive stresses.

Note that the model predicts life using a damage initiation criterion, based on a cyclic softening (stress drop) threshold, and assuming that damage-initiation corresponds to 80% of total life. Damage is defined to initiate when $R = Q_t$, where Q_t is found to be well-represented by a constant value, based on calibration against P91 PM test data across a range of temperatures and strain-ranges [27]. In Fig. 8, damage growth is represented by an equation of the form $\dot{D} =$

$a_7|\dot{p}|$ to simulate the rapid reduction in stress near the end of uniaxial specimen life. For the current work, attention is focused on prediction of damage-initiation.

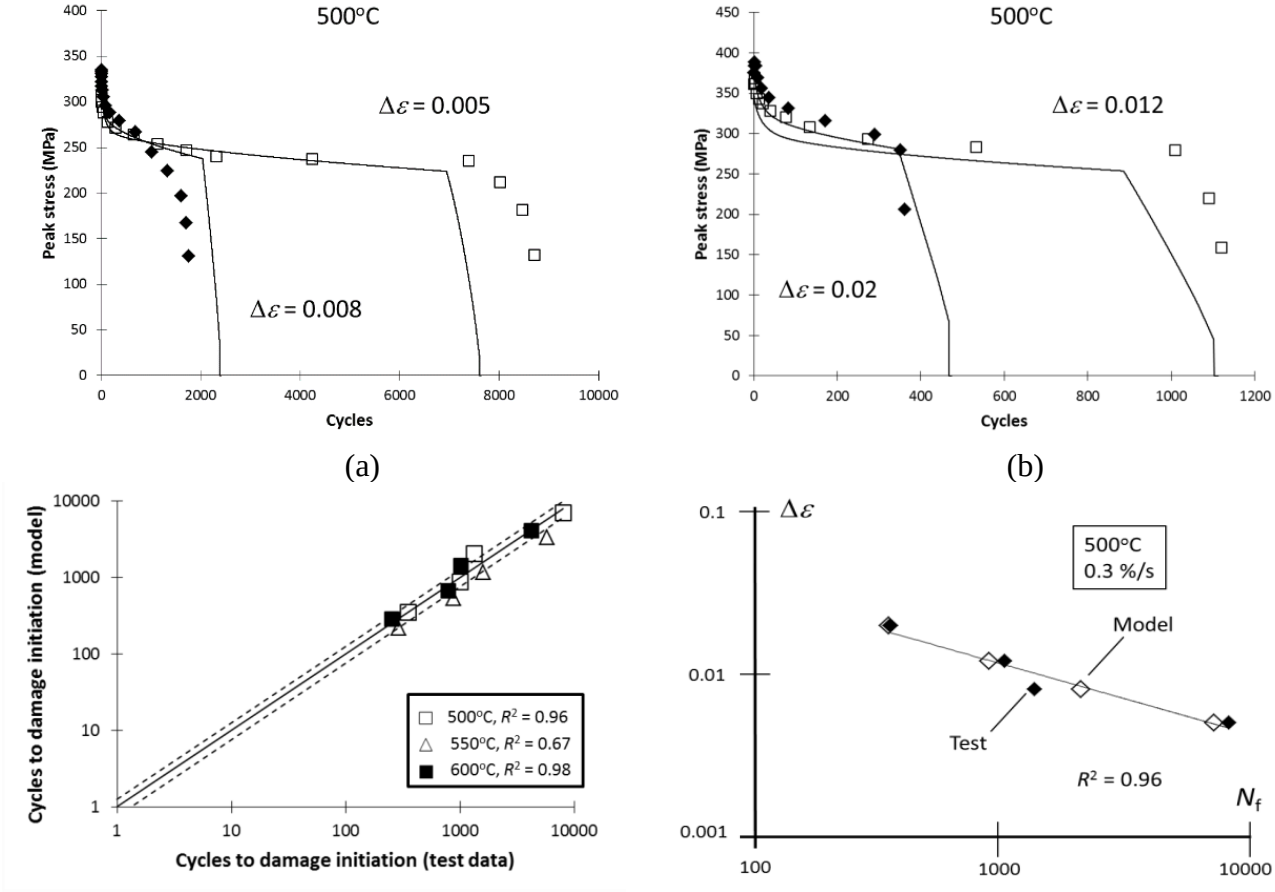

Fig. 8. Calibration of cyclic-softening model against test data [27] at 500°C at strain-ranges of (a) 0.5% and 0.8% and (b) 1.2% and 2%, at constant strain-rate (0.3% s^{-1}); comparisons between the experimentally-observed [27] and modelled number of cycles to damage initiation (taken as sudden drop in peak-stress) for (c) strain-ranges of 0.5%, 0.8%, 1.2% and 2% at different temperatures at a strain-rate of 0.3% (dotted lines represent deviations of 25% from perfect match) and (d) sample strain-life results at 500°C.

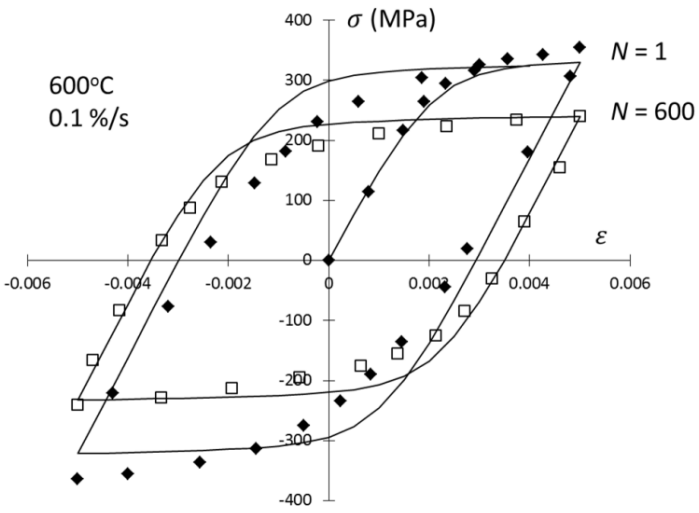

Fig. 9. Validation of model with HTLCF data for P91 PM [11] (points) for 1st and 600th cycles at 600°C (strain-rate 0.1%/s, strain-range 1%).

4. Experimental results

Optical microscopy images, using an optical stereomicroscope, specifically the Olympus SZX10, for PM, simulated HAZ and simulated HAZ with PWHT are shown in Fig. 10, along with optical microscopy of FGHAZ from a P91 welded joint [28]. In Fig. 10a, the PM shows the expected hierarchical microstructure with clear striations indicating the orientation of blocks and packets. The as-welded HAZ (Fig. 10b) shows refinement of the microstructure, consistent with PAG and lath refinement in the FG-ICHAZ.

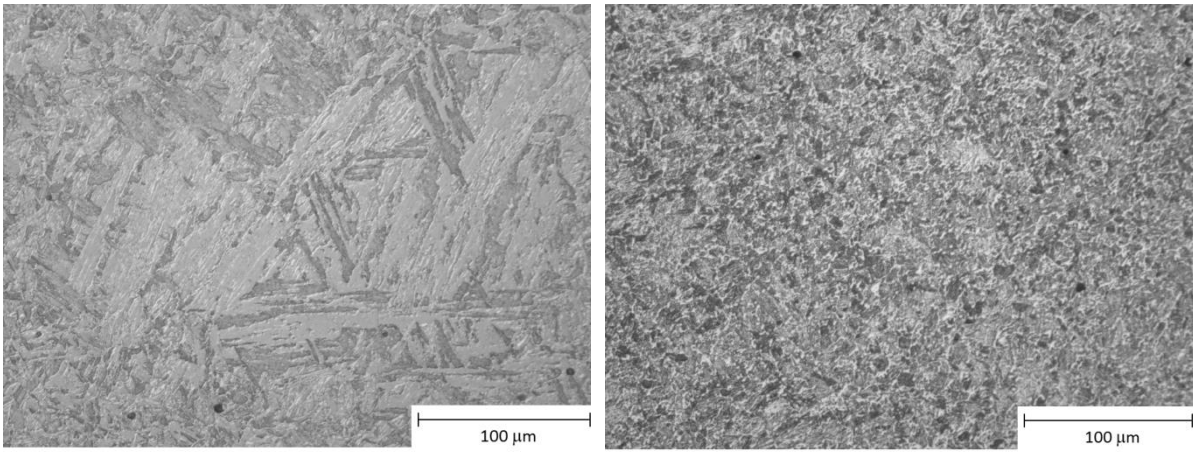

(a) (b)

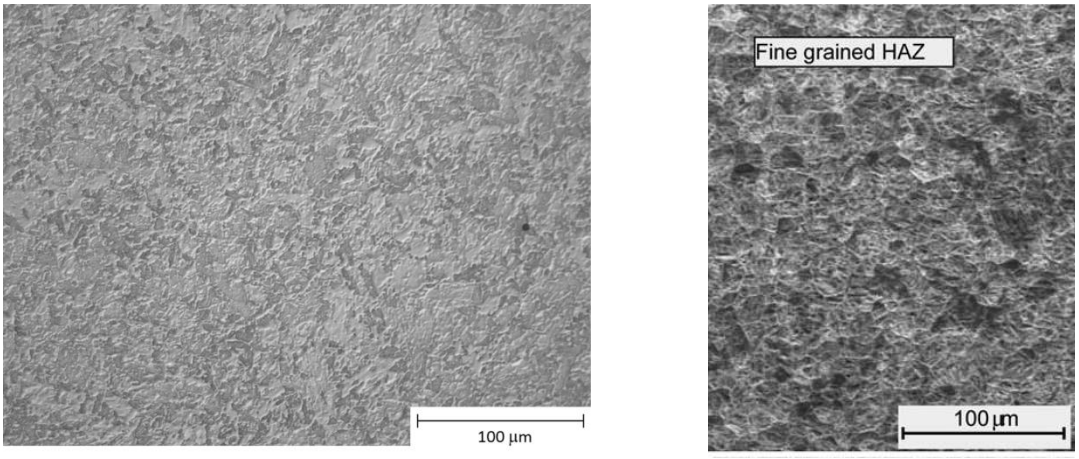

(c) (d)

Figure 10. Optical micrographs of the (a) PM, (b) simulated ICHAZ (AW) and (c) simulated ICHAZ (PWHT) with (d) FGHAZ [28].

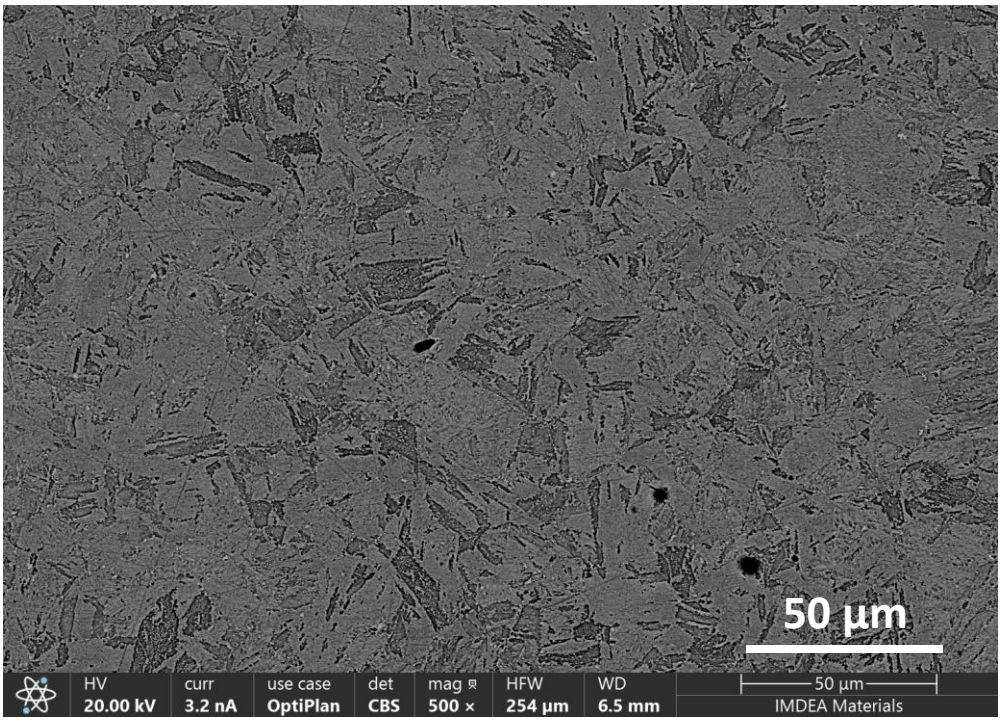

(a)

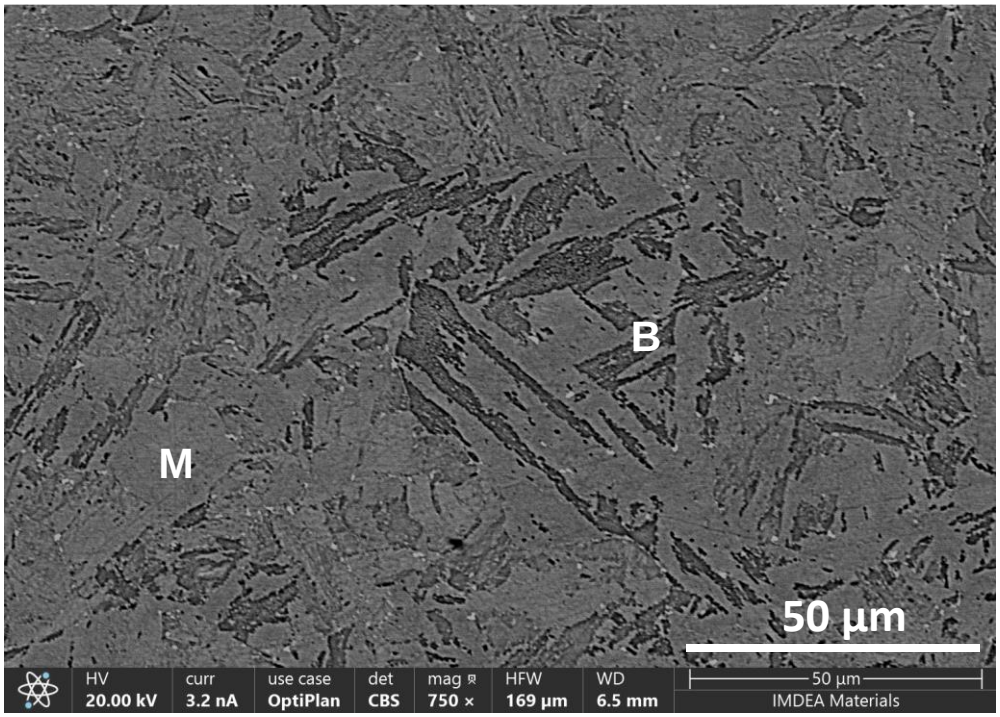

(b)

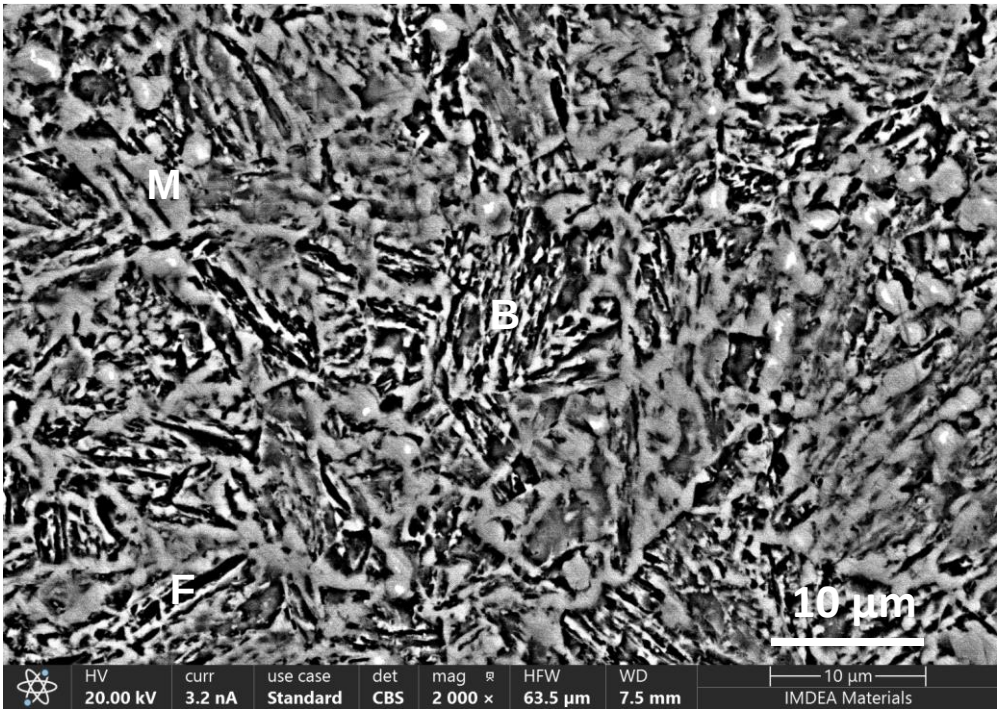

(c)

Fig. 11. Backscattered electron detector SEM images of base material (a, b) and (c) simulated as-welded ICHAZ microstructure.

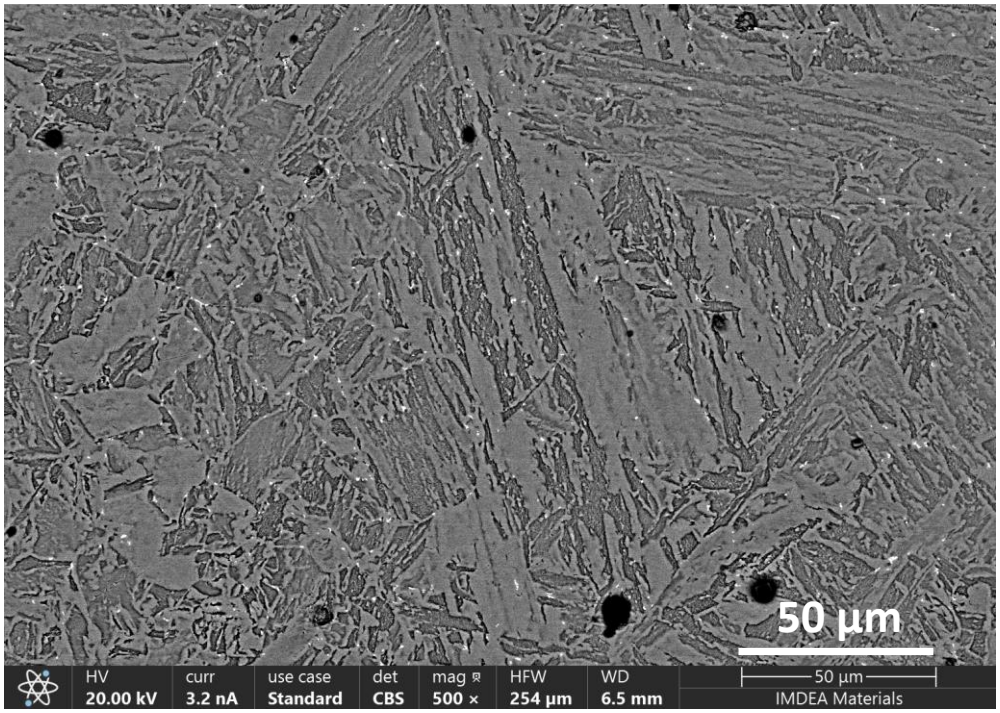

a)

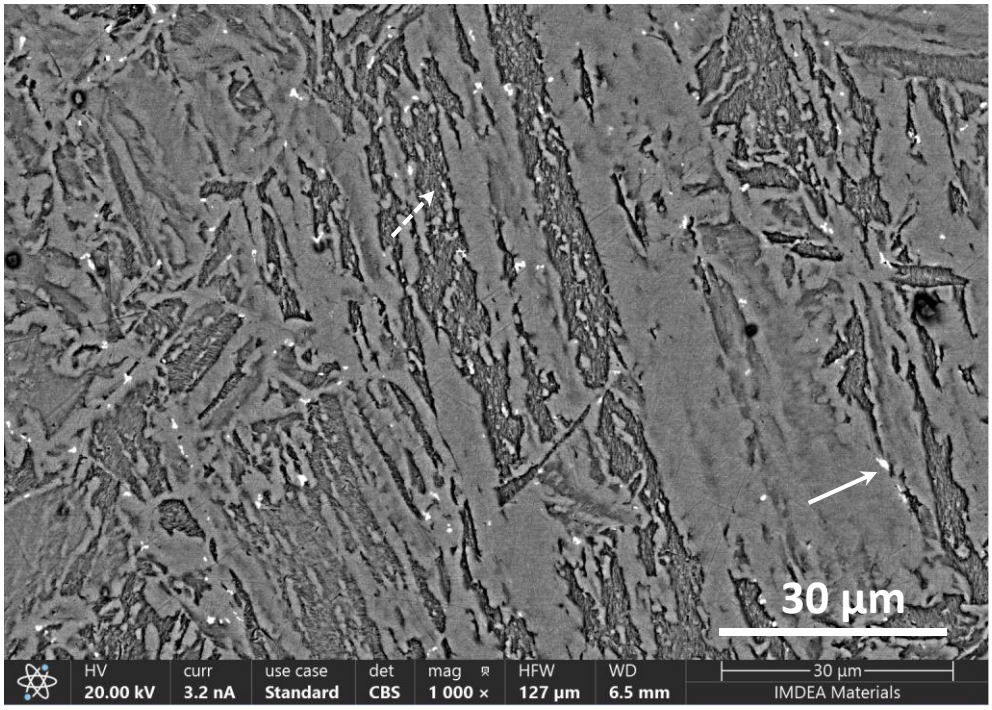

b)

Fig. 12. Backscattered electron detector SEM images of the simulated PWHT ICHAZ microstructure.

Scanning electron microscopy (SEM) analysis of the material before heat treatment revealed a martensitic-bainitic microstructure (Figs 11a, b). The average prior austenite grain size is estimated to be between about 35 μm and 45 μm. SEM of simulated ICHAZ in Figure 11(c) reveals a complex multiphase microstructure consisting of martensite (M), bainite (B) and ferrite (F). This is due to partial ferrite-austenite transformation in the intercritical temperature range. Martensite and bainite are formed from austenite during rapid cooling. The prior austenite grain size is between 15 and 25 μm. ICHAZ microstructures are typically more refined compared to CGHAZ [29]. Similar HAZ microstructures have been previously reported for this material [29, 30]. The PWHT process appears to have produced a less refined microstructure, consistent with lath-recovery (Fig. 12). Tempered martensite and tempered bainite are clearly seen. Furthermore, numerous carbides having a size ≤ 1 μm (white particles in Fig. 12) are observed. The coarser particles are $M_{23}C_6$ carbides, where M is predominantly Cr, Fe and Mo [31] and formed at grain boundaries (marked by solid arrow on Fig. 12b). Finer particles, observed mainly in the intra-lath regions are MC type precipitates, where M is V, Cr and Mo [31] (marked by dashed arrow on Fig. 12b). Similar microstructures have been reported for PWHT P91 steel [29].

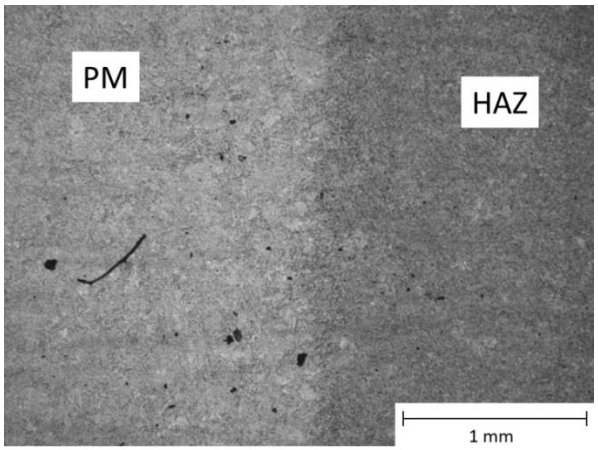

(a)

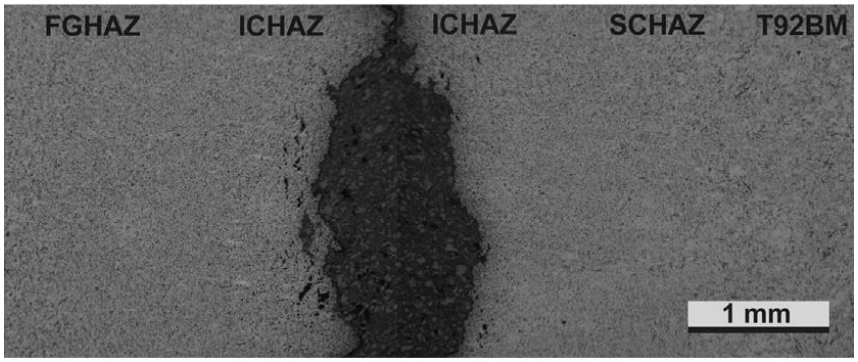

(b)

Fig. 13. Comparison of the microstructure across the HAZ for (a) the present work and (b) a comparison with a T92 welded joint [32].

Comparison with microscopy results for similar material at the same resolution [12], shows clear resemblance between the simulated HAZ from the present work and the FGHAZ from a welded joint. At a lower resolution, Fig. 10, there is clear resemblance between the simulated HAZ generated in the Gleeble and the IC-FGHAZ in a P92 welded joint [32].

During the test, it was found that temperature-control was stable. However, due to extensometer slippage problems on the gauge region, it was decided to use the Gleeble rig itself to control strain, based on crosshead stroke displacement. The cyclic evolution of maximum and minimum stresses in each cycle for the six tests are shown in Figs. 14 and 15.

The numbers of cycles to failure for the TMF testing of PM and simulated ICHAZ are summarised in Table 6. The ICHAZ (AW) material had the longest TMF-IP and TMF-OP lives and also, following some initial transient hardening or softening (depending on IP, OP tension or compression), shows the highest cyclic stress. The ICHAZ (AW) specimens exhibit early-stage hardening (within the first 100 or so cycles) followed by significant gradual softening over the subsequent 150 or so cycles, followed finally by rapid softening associated with failure at about 277 cycles. OP is found to be detrimental relative to IP for the PM and ICHAZ (AW) materials, with significant reductions in TMF life for the TMF-OP case relative to the TMF-IP

case. These results are generally consistent with those obtained by other authors for TMF loading [33]. The ICHAZ (PWHT) case, however, has a similar TMF life for both OP and IP, with IP life being slightly shorter. ICHAZ (PWHT) is seen to be either cyclically softer than or similar to PM in terms of peak tensile or compressive cyclic stress.

Table 6. Results of the P91 TMF testing regime

Material	TMF cycle	N_f
PM	IP	365
PM	OP	118
Simulated ICHAZ (AW)	IP	562
Simulated ICHAZ (AW)	OP	277
Simulated ICHAZ (PWHT)	IP	173
Simulated ICHAZ (PWHT)	OP	196

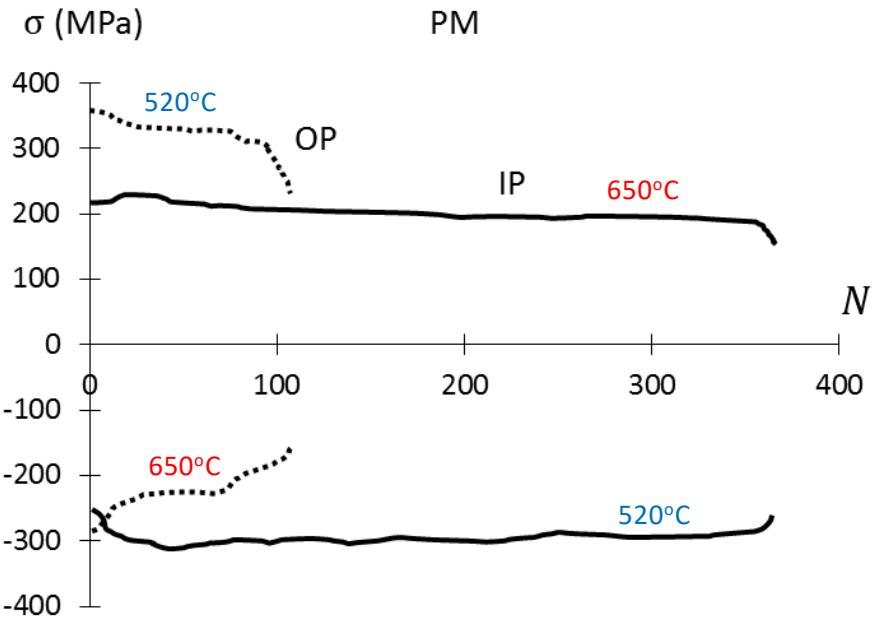

(a)

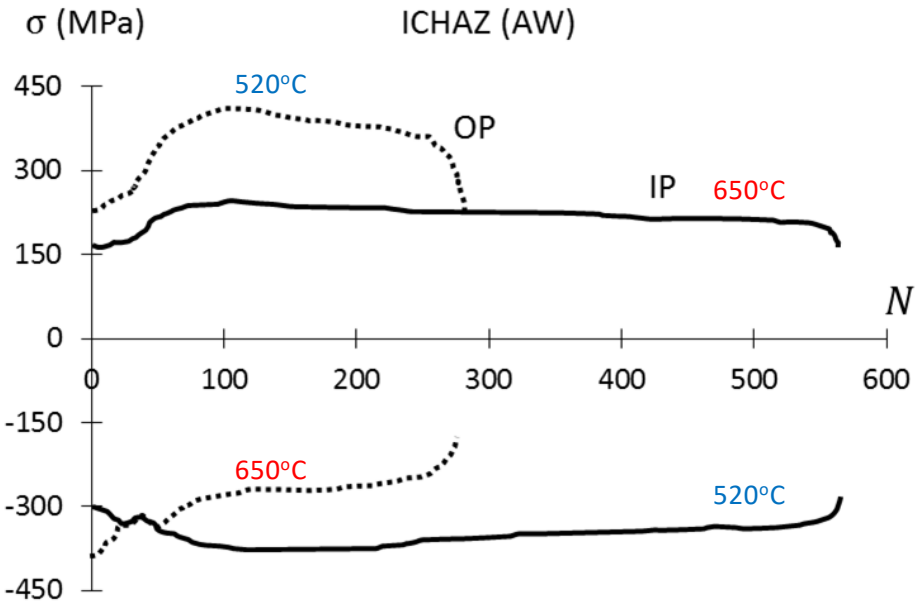

(b)

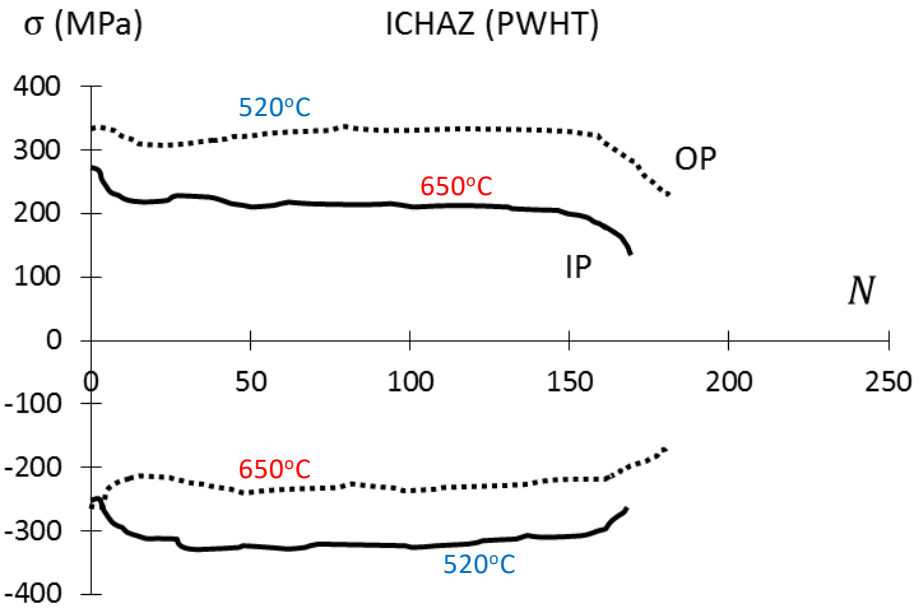

(c)

Fig. 14. Measured cyclic evolutions of maximum tensile and compressive stress in each cycle for the (a) out-of-phase and in-phase TMF responses for PM, (b) out-of-phase and in-phase TMF responses for as-welded ICHAZ and (c) out-of-phase and in-phase TMF responses for PWHT ICHAZ.

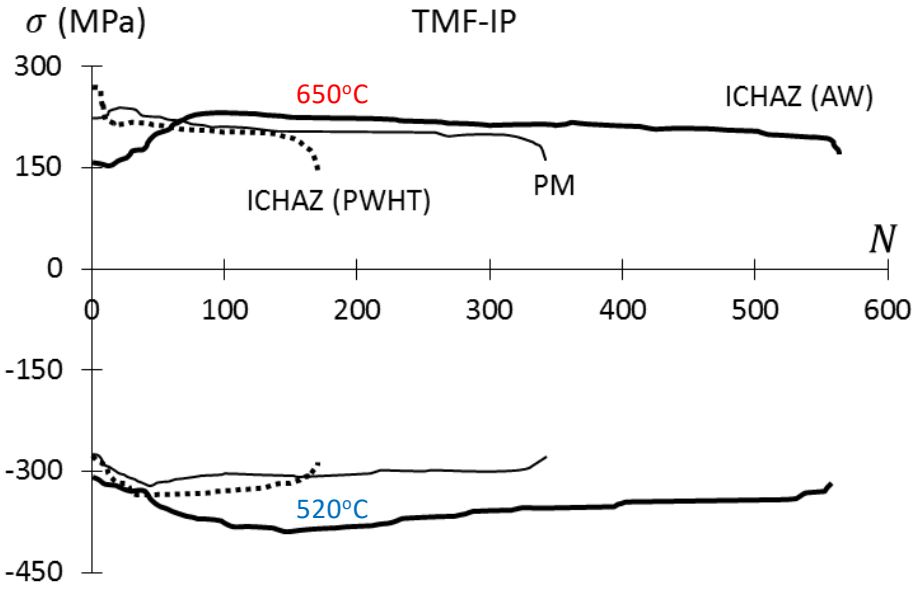

(a)

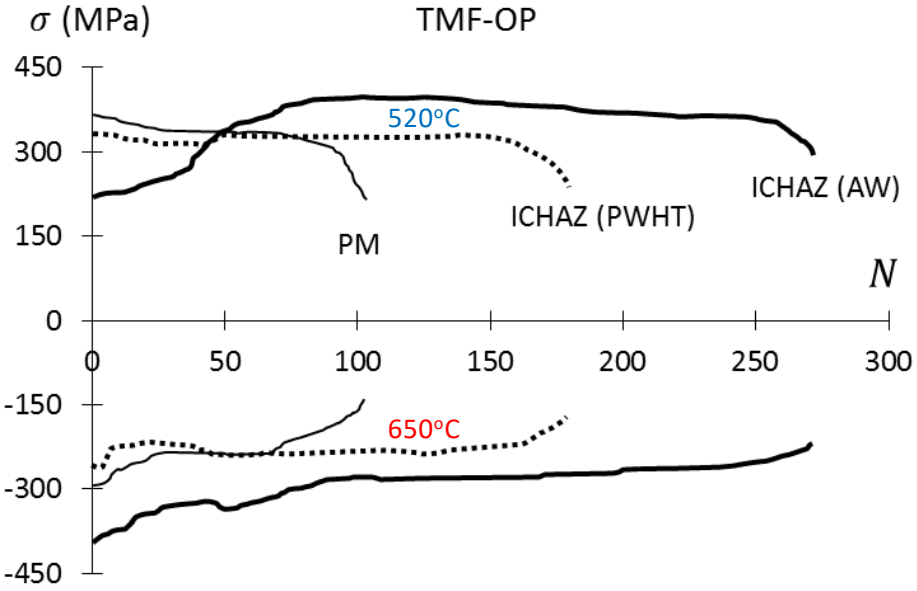

(b)

Fig. 15. Measured cyclic evolutions of maximum tensile and compressive stress in each cycle for PM, ICHAZ (AW) and ICHAZ (PWHT) for (a) TMF-IP and (b) TMF-OP tests.

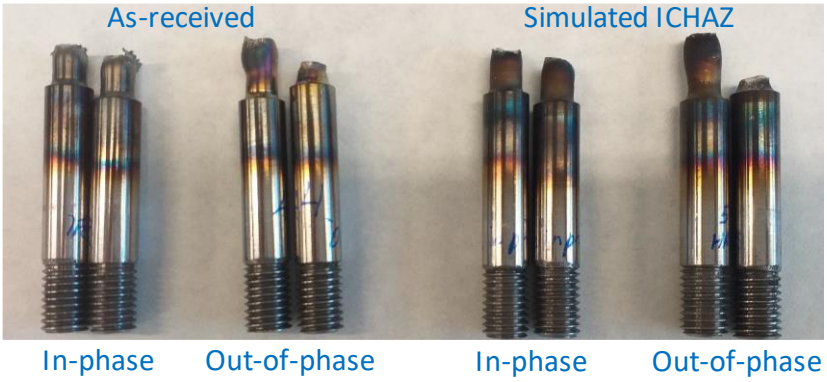

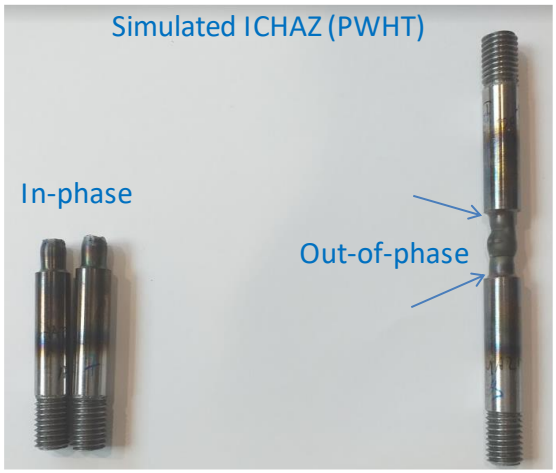

Figure 16. Photographs of samples (a) after thermo-mechanical fatigue testing (as-received and HAZ treated samples) and (b) (HAZ + PWHT treated samples). Circumferential cracks formed on the surface of 'out-of-phase' sample are marked by arrows.

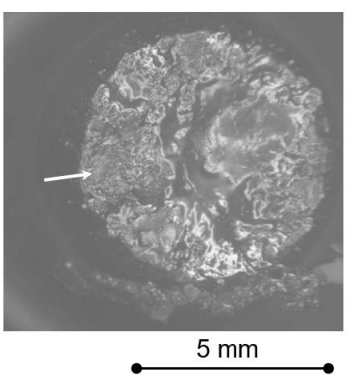

(a) TMF-IP for PM

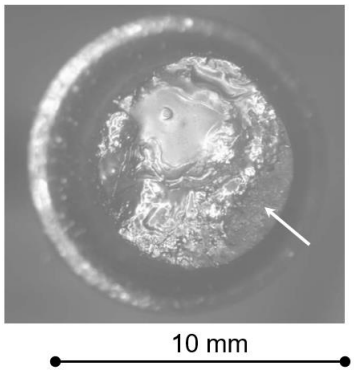

(b) TMF-OP for PM

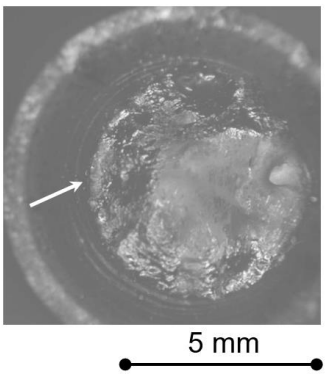

(c) TMF-IP for ICHAZ (AW)

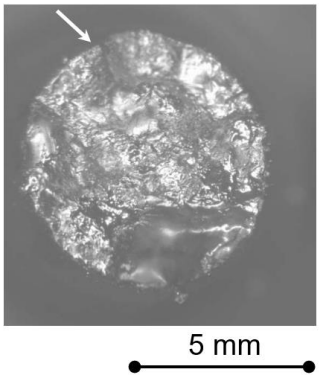

(d) TMF-OP for ICHAZ (AW)

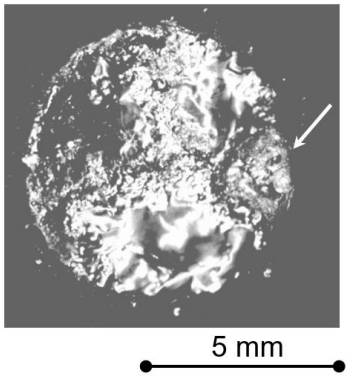

(e) TMF-IP for ICHAZ (PWHT)

Figure 17. Optical microscopy images of fracture surfaces of (a) IP PM, (b) OP PM, (c) IP ICHAZ (AW), (d) OP ICHAZ (AW) and (e) IP ICHAZ (PWHT) test specimens. White arrows indicate crack initiation location.

Figure 16 shows the specimens after testing. The fracture surfaces were analyzed using an optical stereomicroscope, specifically the Olympus SZX10. The fracture surfaces are shown in Figure 17. The TMF-OP ICHAZ (PWHT) specimen did not fracture during the test but it is clear from Fig. 14b that is was approaching failure. The specimens experienced ductile failure, with well-defined crack-initiation zones, followed by a smooth area of sudden fracture. For the in-phase tests (Fig. 17a, 17c and 17e), the crack-initiation and propagation regions account for a greater proportion of the cross-sectional area than for the out-of-phase tests. Furthermore, the fracture region for the IP ICHAZ (AW) is the smallest of the four specimens, corresponding to the longest TMF life. The specimen with the most clearly-defined fracture region, the OP PM specimen (Fig. 17b), had the shortest TMF life.

5. Material model results

The present through-process, physically-based model has been adopted for computer simulation of the Gleeble physical welding and PWHT simulations. Table 7 shows a comparison of the initial identified PM microstructure parameters for the model and the model-predicted corresponding values for AW ICHAZ and PWHT ICHAZ.

Table 7. Initial specified and predicted microstructure parameters for thermal-metallurgical-mechanical model for HTLCF and TMF simulations.

Parameter	PM	ICHAZ (AW)	ICHAZ (PWHT)
PAG size (μm)	35	12	12
$M_{23}C_6$ diameter (nm)	76	56	85
$M_{23}C_6$ area fraction (%)	4.5	3.3	5.2
Vickers hardness (kgf/mm^2)	220	450	219.5
Lath width (nm)	600	38	617

In order to validate the material model, comparisons are presented against previously published TMF testing results for ES-P91 PM, for both symmetric and non-symmetric TMF testing between 400^{o}C and 600^{o}C as follows:

(i) symmetric TMF-IP and -OP tests, for ± 0.5% strain range,

(ii) non-symmetric TMF-OP for strain-range from +0.4% to -0.1%,

(iii) non-symmetric TMF-IP for strain-range from +0.5% to -0.2%, and

(iv) non-symmetric TMF-OP for strain-range from +0.4% to -0.1%.

Figure 18 shows sample comparisons of the model predictions for the initial hysteresis loops for these symmetric TMF cases between 400^{o}C and 600^{o}C and for isothermal HTLCF at 400^{o}C, and the maximum and minimum cyclic stress envelope for the TMF cases. Figure 19 shows test data results [24] and model predictions for the non-symmetric TMF loading for the same temperature-range. Figure 20 shows the strain-life plots for the test data and the model predictions. Note that the model life is predicted using damage initiation and then assuming that the damage-initiation life corresponds to 80% of total life.

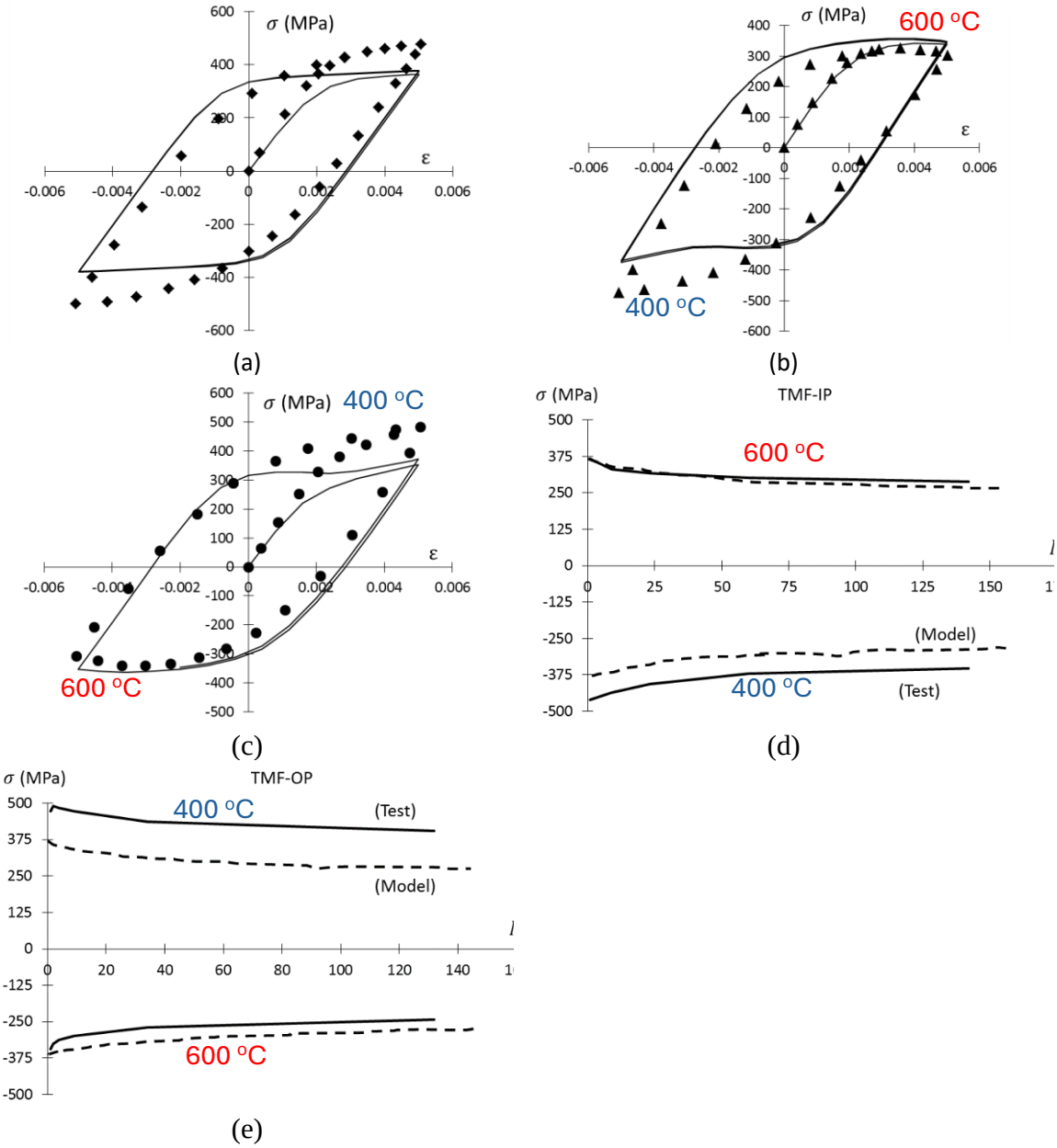

Figure 18. Comparison of test data and the model for P91 PM (a) isothermal fatigue at 400°C, (b) TMF-IP and (c) TMF-OP between 400°C and 600°C, as well as stress versus cycles for (d) the TMP-IP case and (e) the TMF-OP case. Note, results for (a) to (c) are for the first fatigue cycle, $N = 1$.

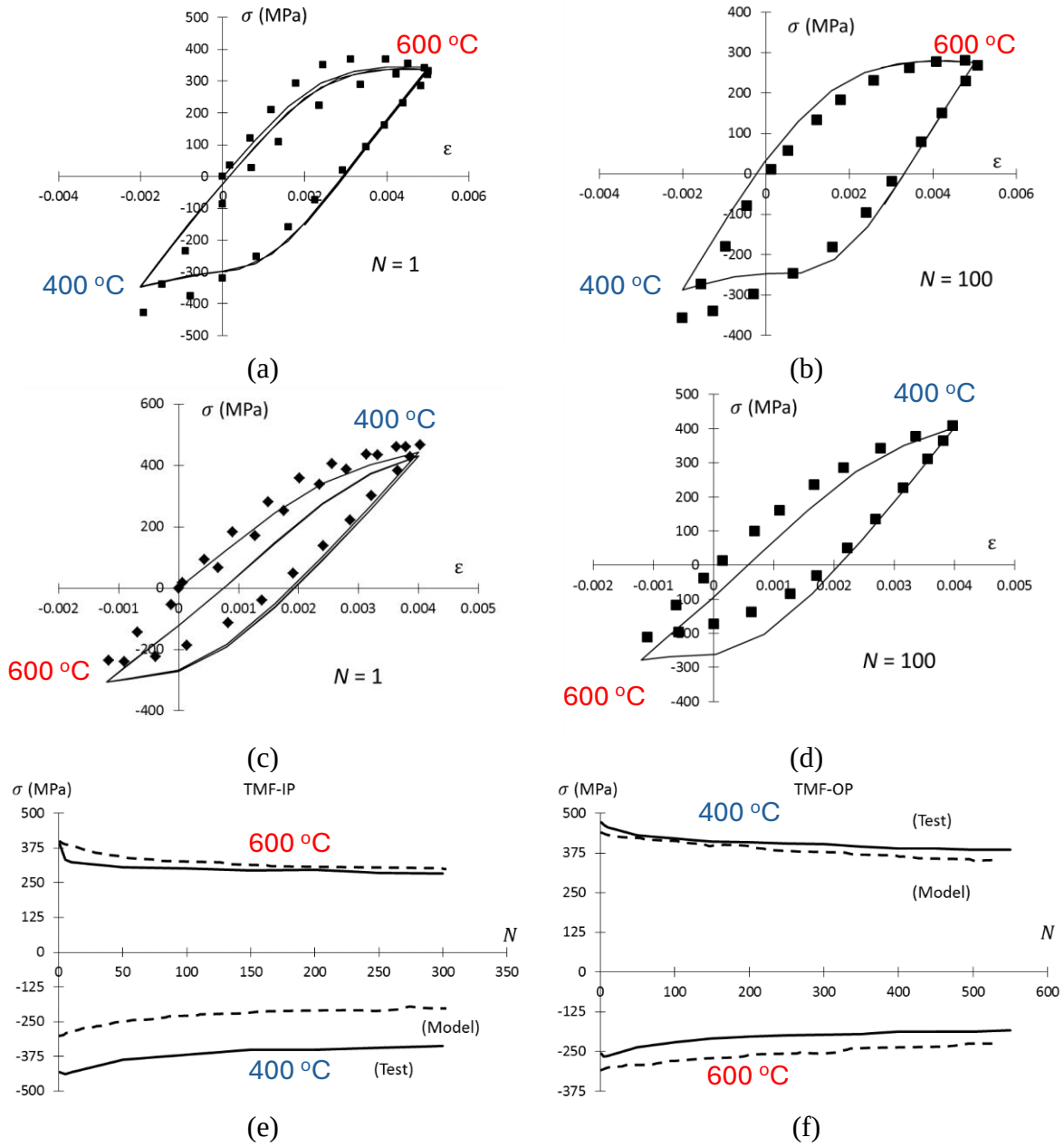

Figure 19. Comparison of TMF test data (points) and the model for P91 PM between 400°C and 600°C: (a) $N = 1$ and (b) $N = 100$ non-symmetric TMF-IP for strain-ranges of +0.5%, -0.2% and (c) $N = 1$ and (d) $N = 100$ non-symmetric TMF-OP for strain-ranges of +0.4%, -0.1%, with stress versus cycle comparison for (e) TMF-IP for strain-ranges of +0.5%, -0.2% and (f) TMF-OP for strain-ranges of +0.4%, -0.1%.

Damage initiation is represented using a damage-indicator parameter that is based on cyclic softening rather than using the dislocation-density based monotonic damage of the previous chapter. This resulted in a significant reduction in number of modelling parameters while

maintaining the applicability of the model for in-service life prediction of power plant components. It was assumed that relatively large plastic strains associated with monotonic damage would not occur in power plant components. Damage is defined to initiate when $R = Q_t$, where Q_t is found to be well-represented by a constant value, based on calibration against P91 PM test data across a range of temperatures and strain-ranges [27]. In Fig. 9, damage growth is represented by an equation of the form $\dot{D} = a_7|\dot{p}|$ to simulate the rapid reduction in stress near the end of uniaxial specimen life. For the current work, attention is focused on prediction of damage-initiation.

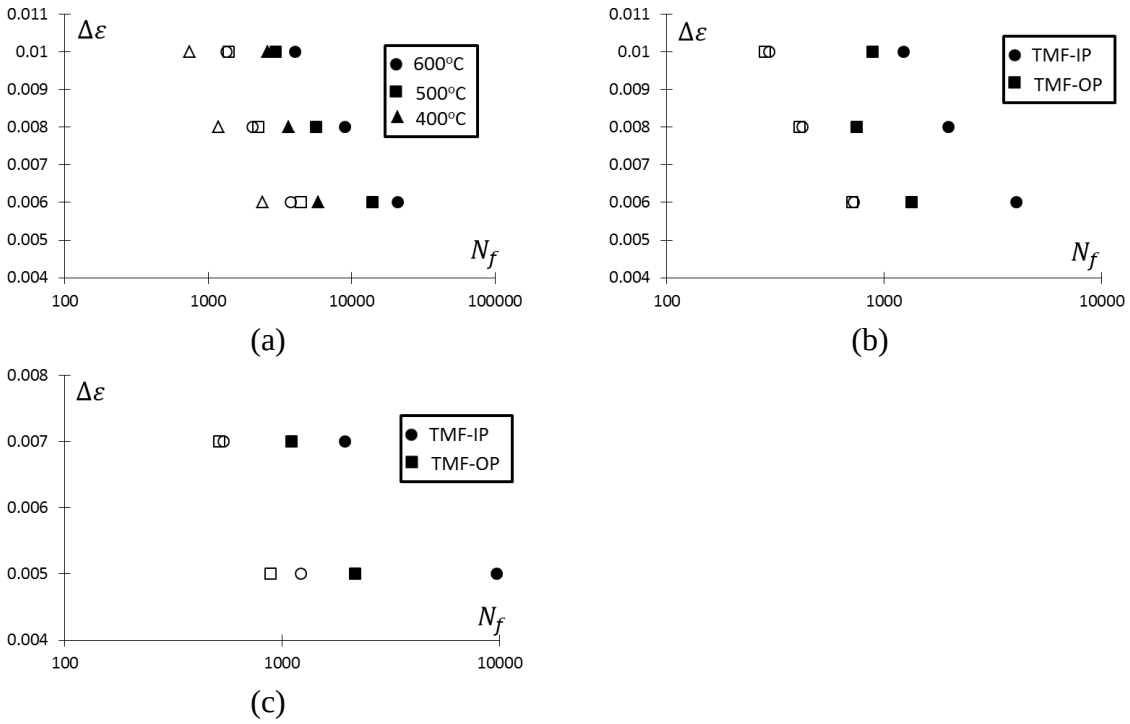

Figure 20. A comparison of predicted (hollow points) and observed (solid points) number of cycles to failure for (a) isothermal HTLCF, (b) symmetric TMF between 400°C and 600°C, and (c) non-symmetric TMF between 400°C and 600°C (IP: +0.5%, -0.2%, OP: +0.4%, -0.1% strain).

Figures 21 to 23 show the model predictions of cyclic evolutions of maximum tensile and minimum compressive stresses for PM, ICHAZ (AW) and ICHAZ (PWHT).

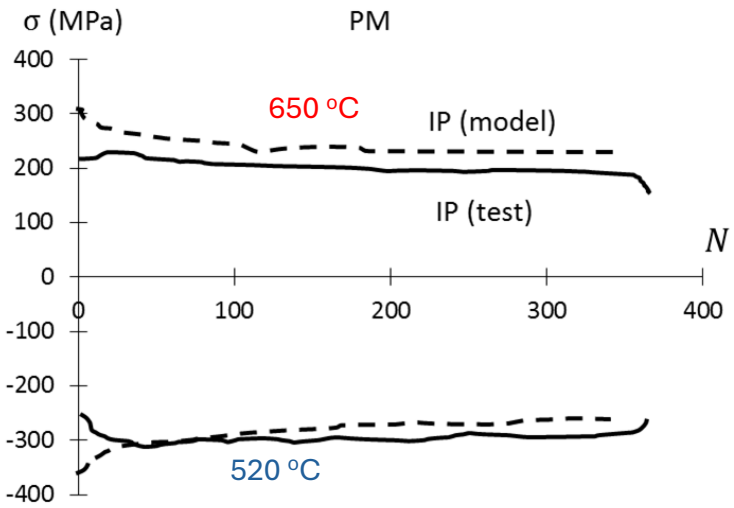

(a)

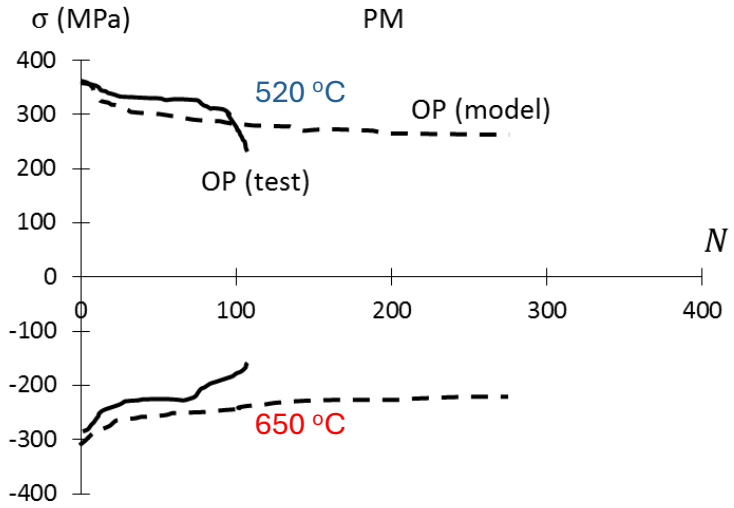

(b)

Fig. 21. Comparison of model and test cyclic evolutions of maximum tensile and compressive stresses per cycle for (a) TMF-IP PM and (b) TMF-OP PM tests.

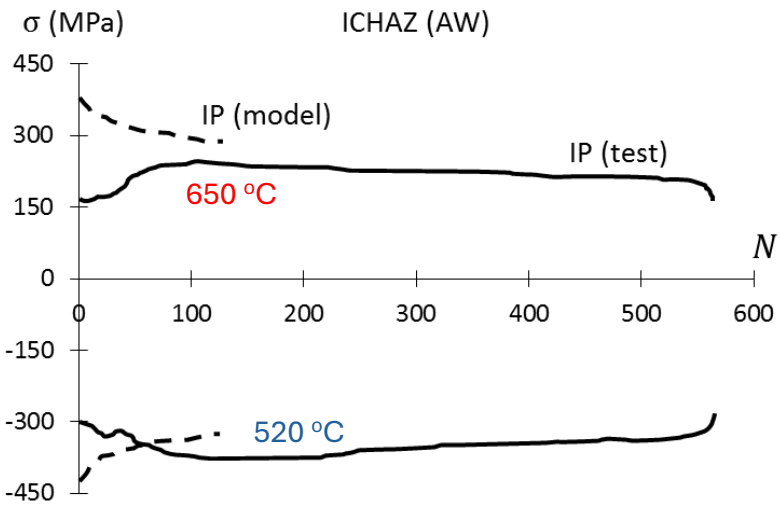

(a)

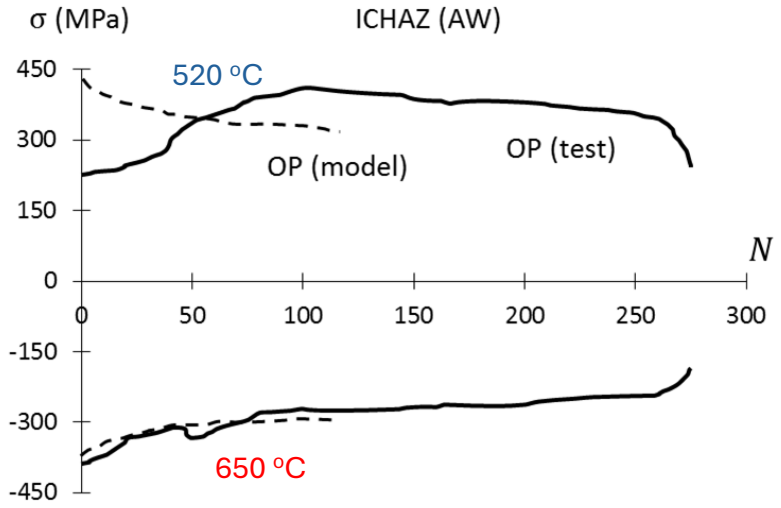

(b)

Figure 22. Comparison of model and test cyclic evolutions of maximum tensile and compressive stresses per cycle for ICHAZ (AW): (a) TMF-IP and (b) TMF-OP.

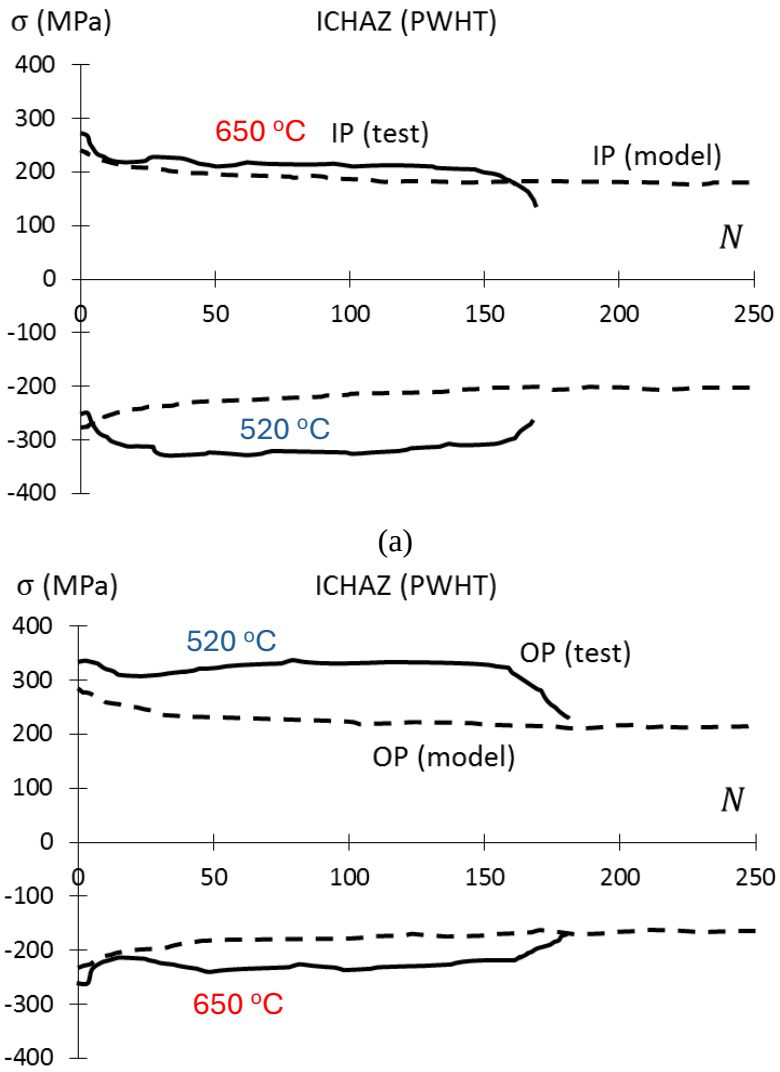

(a)

(b)

Figure 23. Comparison of model and test data evolution of maximum tensile and compressive stress per cycle for (a) TMF-IP ICHAZ (PWHT) and (b) TMF-OP ICHAZ (PWHT) tests.

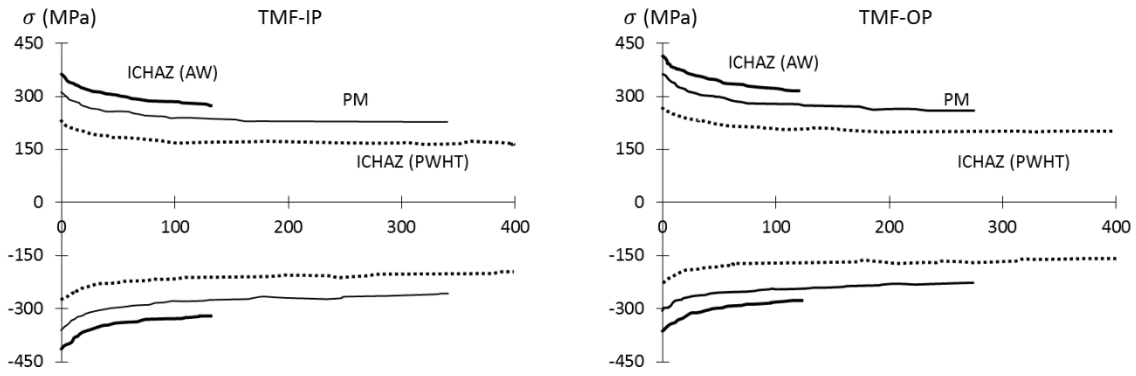

(a)

(b)

Figure 24. The model predicted cyclic evolutions of maximum tensile and compressive stress per cycle for PM, simulated ICHAZ (AW) and simulated ICHAZ (PWHT) for (a) TMF-IP and (b) TMF-OP test conditions.

4. Discussion

This work presents the in-situ Gleeble physically-simulated welding with combined TMF testing up to 650^{o}C of P91 material for parent material, inter-critical heat affected zone, as-welded and pow-weld heat treatment. A previously presented process-structure-property model was adapted and applied to the combined simulated welding and TMF testing, as well as previously-presented high temperature low cycle fatigue and TMF testing to 600^{o}C.

Of key importance is the testing of ICHAZ material, for which a suitable thermal cycle had to be identified in order to produce ICHAZ specimens during simulated welding tests. The microscopy comparisons shown in Figs. 10 to 12 give confidence that the simulated welding produced microstructure representative of ICHAZ. The material used to provide specimens was machined such that they were free of WM or HAZ so that each specimen was nominally identical in terms of microstructure. The geometry of the specimens was chosen based on best-practice and experience.

In previous work [23], where we have developed models for thermo-mechanical analysis of high temperature, steam-pressurised P91 pipes in electrical power generation plant under realistic (measured) temperature and pressure cycles, it was shown that in plain pipes (without stress concentration features, such as welds) cold-start and other typical thermal cycle predictions lead to significant cyclic inelastic strains of at least 0.2 %, with compressive (hoop) strains resulting from inside pipe surface heat-up and tensile (hoop) stresses and inelastic strains being driven by inside surface cool-down. For welded pipes, with significant stress concentrations features, larger cyclic inelastic strains can be expected under realistic thermo-mechanical conditions.

It is well known that 9Cr steels (PM) generally exhibit cyclic softening during high temperature cyclic deformation, as discussed in detail by Barrett et al. [35], for example, primarily attributed to the coarsening of the martensitic lath microstructure, reduction of initial high dislocation density, and carbide coarsening. Hence, as discussed in Section 3, and previously in cited work by MacArdghail, Leen and co-workers, the model represents this cyclic softening, via the microstructure evolution, particularly for the final stage where failure occurs. A key aspect of the present work is to investigate the ability of the thermal-metallurgical-mechanical model for the present Gleeble simulation of TMF of P91 HAZ. The model was previously applied to simulation of multi-pass welding and subsequent HTLCF behaviour and was successfully demonstrated [6] to achieve consistent behaviour in terms of weld life reduction factors for HTLCF of P91 welded uniaxial test specimens at 600 degC and 2% strain range [36]. However, for the HAZ of the present work, even though subsequent gradual softening is displayed, some initial transient hardening is displayed by the HAZ tests; eventually leading to softening associated with cyclic failure. To the authors' knowledge, this is the first time that P91 ICHAZ material has been isolated for high temperature cyclic testing (e.g. TMF or HTLCF); this was possible via the Gleeble physical simulation. A key finding of the present work is that although the PM (test and model) displays expected behaviour in terms of cyclic softening from early cycles, the as-welded HAZ (test) displays initial hardening, whereas the model assumes softening; in contrast, the PWHT HAZ displays behaviour more consistent with PM and the model also performs more consistently for these cases. From a microstructural perspective, there is evidence from the work of Abe et al. [37] to indicate that it is possible to obtain HAZ without lath structure (e.g. ferrite), specifically for simulated HAZ material generated by heating close to or above the Ac3 temperature (920 degC), as in the present work (in fact, this was shown to be the cause of Type IV cracking in creep testing of 9Cr steel ICHAZ, after

PWHT). There is a need to improve the modelling, in future work, to address the possibility of formation of ferrite and associated hardening, for example.

In Fig. 14, the test results are presented by material and in Fig. 15, by the TMF-IP and TMF-OP test conditions. Fig. 14a shows the typical TMF-OP response for PM, whereby the stress is non-symmetric, i.e. the magnitude of maximum tensile stress is higher than that of maximum compressive stress. This is attributable to the harder material response at the lower temperature of 520 ^{o}C during the tensile phase and softer material response at the higher temperature of 650 ^{o}C during the compressive phase. In contrast, for the TMF-IP response, the stress is non-symmetric in the opposite way, i.e. large compressive stress during low temperature phase and lower tensile stress during high temperature phase. As expected for P91 material, cyclic softening occurs for the TMF-OP with accelerated softening immediately preceding failure and, in general, also for the TMF-IP condition, apart from some initial transient hardening during the very early 10 or so cycles. For the PM (tempered martensite) case, the high bulk density of LAB (low angle boundary) dislocations results in a net decrease in overall dislocation density, and hence, cyclic softening behaviour, following the Taylor hardening model, for example. Also, as expected for TMF-OP, due to the higher maximum tensile stress, the number of cycles to failure for OP is significantly less than for IP (118 cycles compared to 365 cycles). Fig. 14b shows that the simulated ICHAZ (AW) tests also show the same TMF-OP non-symmetric effects with higher tensile stress for lower temperature phase and vice-versa for IP, and associated significantly reduced life for OP (277 cycles compared to 562 for IP). In this case, both OP and IP tests exhibit initial cyclic hardening (in OP and IP tension and in OP compression only) during the first 100 or so cycles, followed by the more typical (gradual) cyclic softening associated with 9-12 Cr steels, with accelerated softening immediately preceding failure. The initial cyclic hardening may be attributed to the presence of ferrite and

absence of a lath structure in the ICHAZ, leading to reduced overall dislocation density (relative to the same material undergoing 100% austenitic microstructure before rapid cooling for the martensitic transformation), and hence, enabling a net increase in dislocation density (bulk work hardening) as the opportunity for LAB dislocation annihilation is reduced with increasing ferrite content. The TMF lives for the ICHAZ (AW) material are significantly longer than for PM. Figure 14c shows that, for simulated ICHAZ (PWHT) material, the expected TMF phenomenon of higher maximum tensile stress for OP and higher maximum compressive for IP occurs again, although, in this case, the IP life is actually slightly lower than the OP life. The IP case shows some initial hardening for the compressive (low temperature) phase over the first 25 or so cycles. In general, this material displays fairly stabilised response over the duration of the tests, until significant softening immediately preceding failure. In the case of the PWHT ICHAZ sample, the effect of initial hardening is substantially reduced, compared to that of the as-welded ICHAZ sample. Although the volume fraction of ferrite is expected to remain approximately constant following the PWHT process, with only the bct (body centred tetragonal) martensite transforming into bcc (body centred cubic) tempered martensite, the reduction in early-stage cyclic hardening for this case compared to the as-welded ICHAZ sample is attributed here to increased plastic strain compared to the as-welded material, and therefore, increased plastic-strain driven LAB dislocation density annihilation, resulting in increased cyclic softening (reduced hardening). The increased plastic strain compared with the case of the as-welded ICHAZ result is due to a reduction in yield strength with PWHT as (i) dislocation density is reduced, and (ii) MX and Cr-rich $M_{23}C_6$ particles form at the expense of C, Mo and Cr solutes. Figure 15 shows that, after the first 50 or so cycles, for both OP and IP test, the ICHAZ (AW) material has a harder response (i.e. higher maximum tensile and compressive stresses) than ICHAZ (PWHT) and PM materials, particularly for the OP

condition; for the earlier cycles, it is significantly softer. The AW material also has a significantly longer life.

It should be noted that the material in question is simulated ICHAZ, and not a welded connection (e.g. cross-weld specimen), and therefore lacks certain features of welded connections, such as adjacent hard and soft material regions causing strain incompatibilities, leading to cracking [37]. The presence of such a hardened material region in a welded joint will weaken the joint as a whole, even if a specific material region is itself stronger due to the welding process. Furthermore, the simulated ICHAZ (AW) material lacks PWHT and is the result of a single thermal cycle, and therefore is not precisely representative of welded plant material, which typically experiences PWHT and is produced by multi-pass welding, with associated effects of auto-tempering to soften the ICHAZ, even without PWHT.

PWHT leads to a more homogeneous material across the welded joint as a whole and reduces residual stresses, but can result in the ICHAZ being the softest material region and therefore the source of weakness for the joint as a whole, as has been the industry experience. In this work, the simulated ICHAZ (PWHT) is found to have a reduced TMF life compared to the PM for the TMF-IP case (Fig. 15a). For the TMF-OP case, the PWHT ICHAZ life is similar to that of the PM (Fig. 15b). This indicates that following PWHT, the ICHAZ has comparable or reduced strength compared to the PM, consistent with industry experience [3, 44]. Of course, real welded connections, in addition to welding-induced macro- and micro-scale material inhomogeneities, also typically have geometric discontinuities which cause stress-strain concentrations.

In Fig. 18, it is clear that the model-predicted TMF response is bounded by the isothermal HTLCF response, e.g. for TMF-IP (Fig. 18b) the peak tensile stess is similar to that at 600^{o}C in HTLCF (Fig. 9, first cycle), while the compressive stress is similar to the 400^{o}C HTLCF compressive stress (Fig. 18a). For the TMF predictions, the stress-strain results at higher temperatures match the test data better than at lower temperatures, as to be expected when the TMF response is bounded by the HTLCF responses, e.g. the model underpredicts the 400^{o}C HTLCF stress so it underpredicts the TMF stress at temperatures approaching 400^{o}C. This trend is consistent with increasing numbers of cycles (Figs. 18d and 18e), where there is general agreement for the higher temperature stress but the model underpredicts the stress magnitude at the lower temperature. The model underpredicts IP conpression for 400^{o}C and OP tension for 400^{o}C. For the non-symmetric TMF cycles of Figure 19, the peak tensile stresses are captured reasonably accurately, compared to the peak compressive stresses. The model underpredicts the stress for 400^{o}C compression and over-predicts for 600^{o}C tension. The stress versus cycle results in Fig. 19e again shows general agreement for the high-temperature stresses while Fig. 19f shows general agreement for both tensile and compressive stresses, although it should be noted that the stress-strain loop is predicted to drift relative to the test data (Fig. 19d).

It is clear from Fig. 20 that the model under-predicts TMF life (i.e. conservative) for parent material P91 in the 400^{o}C to 600^{o}C range for all isothermal HTLCF (at 400^{o}C, 500^{o}C and 600^{o}C) and TMF cases, symmetric and non-symmetric, compared to the test data. This can be attributed to the tests being conducted on ex-service material, which is essentially pre-softened with consequent reduced softening-rate, compared to as-received material, against which the model is calibrated. Also, the relatively simple (softening threshold) failure model does not capture the more detrimental effect of OP on life.

In Fig. 21, the model for the PM is seen to slightly over-predict tensile stress but captures the compressive stress quite well for the IP case. This trend is reversed for the OP case. Figure 22 shows the same comparisons for the ICHAZ (AW) tests. In this case, the model significantly over-predicts the early-stage tensile stresses for OP and IP and compressive stress for IP, due to initial lower yield stress and subsequent cyclic hardening of the test sample (apparently due to presence of ferrite and absence of lath structure, as discussed above) compared to assumed softening in the model (the AW-ICHAZ model does not include ferrite and assumes an overly refined lath structure and PAG size); however, the model stresses approach the test values with increasing cycles after about 100 cycles. The model response terminates after significantly fewer cycles, i.e. significant under-prediction of failure life, due to softening threshold for crack initiation ($R = Q_t$) being reached. Figure 23 shows the comparison of model and test for ICHAZ (PWHT). The predicted and measured stress values are in good agreement for the IP test in tension (Fig. 23a) and reasonable agreement for compressive stresses in the OP test (Fig. 23b), corresponding to the maximum temperature conditions. The magnitude of the OP low-temperature stresses is generally under-predicted by the model. For the OP test, this means under-predicting the tensile stress, an important design criterion [34], resulting in a non-conservative prediction.

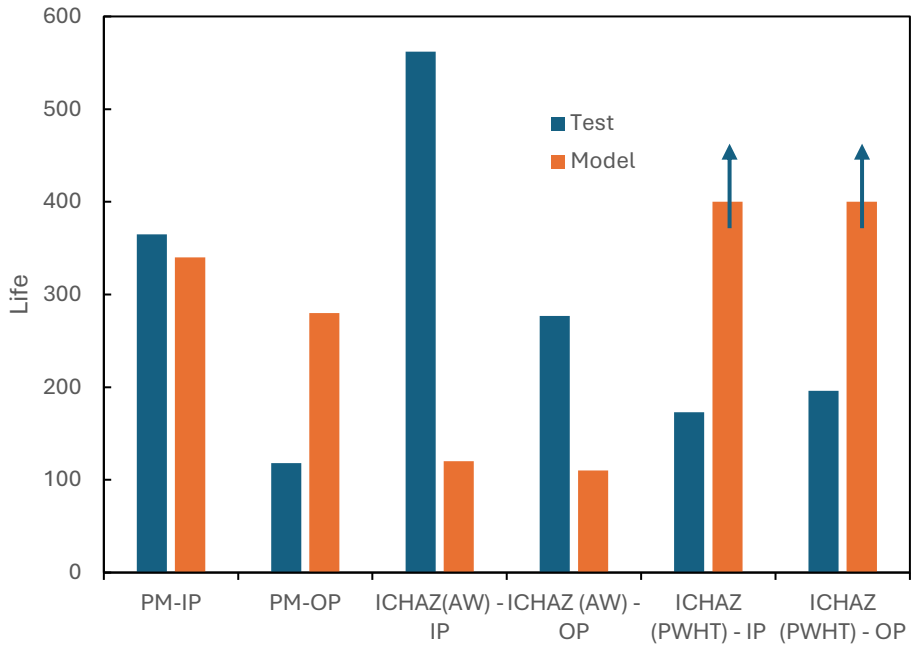

Figure 25. Comparison of measured and predicted TMF lives for PM and simulate ICHAZ, as-welded and with PWHT. Arrows indicate life predicted to be longer than number of cycles simulated.

The effect of material welding condition for model cyclic stress predictions are compared in Fig. 24. It is clear that the ICHAZ (PWHT) is predicted to be softer than the ICHAZ (AW), which is consistent with the stabilised trend in the test results shown in Fig. 15. The model also captured this important general process-structure-property trend of the PM stabilised response being softer than ICHAZ (AW), as also seen in Fig. 15. Figure 25 shows a comparison of the measured and model-predicted TMF lives for the various physically-simulated material conditions considered in the TMF range 520°C to 650°C. It is clear that, in contrast to the HTLCF and TMF results in the range 400°C to 600°C, the relatively simple $R = Q_t$ failure model does not give consistently conservative results. It is conservative for three out of the six cases considered, viz. PM-IP, and ICHAZ (AW), IP and OP. For PM-OP, it is not significantly non-conservative, especially for LCF tests. However, for ICHAZ (PWHT) the failure model significantly over-predicts TMF life. It is clear that significant opportunities exist for improvement of the modelling. Specific examples include HTLCF calibration of the model for temperatures above 600°C, up to 650°C and introduction of an improved physically-based

failure model, suited to TMF, e.g. some type of combination of Tanaka-Mura and perhaps something like Ostergren or Zamrik; improved modelling of material phases, including ferrite; further investigation of microstructure effects during physical simulation of welding and subsequent TMF testing. Incorporation of recent developments of Barrett et al., [24, 35] for example, represents a basis for such developments.

The material model does not explicitly model damage or crack propagation. Other authors have successfully implemented a range of damage models, e.g. continuum [38, 39], mixed ductile and brittle [40], energy-based [41, 42], *S-N* curve-based [43], etc. Such detailed damage modelling is an area for future research and would likely lead to improved agreement between predicted and measured TMF lives. However, the main emphasis of the current work is the inhomogeneity of microstructure-sensitive constitutive behaviour of the different welding-affected materials, rather than the failure behaviour, per se.

A key objective of the research effort which this paper forms part of relates to the development of process-structure-property models for steels, including specifically high temperature steels, such as 9Cr steels for thermal power plant, and with special focus on fatigue of welded connections, including HTLCF and TMF. Previous recent work has demonstrated the successful application of the physically-based modelling methods of Barrett [11, 35] to HTLCF weld life reduction for a welded P91 cross-weld specimen for 400^{o}C and 500^{o}C, based on adoption of the Tanaka-Mura fatigue model, with packet size as the key microstructure parameter; this was essentially a structure-property model, since no attempt was made to predict the microstructure parameters from a welding model. In the present work, we go a step further, by adopting the through-process model of MacArdghail and co-workers [6, 25] to the simulated welding and PWHT process for P91 steel and combined TMF to 650^{o}C; this

inevitably requires some assumptions, described in detail in previous work. One key assumption is that the model links lath width to PAG size and hardness, as well as $M_{23}C_6$ precipitates; hence, the model assumes a lath structure and a mixed phase microstructure, consisting of martensite (tempered and untempered) and austenite. In the case of ICHAZ (AW), the microscopy suggests the absence of a lath structure and the presence of ferrite, as well as bainite. The results of Table 7, compared to the microstructure analysis of Figs. 10 to 12, thus show that the predicted ICHAZ (AW) microstructure is not correct, in assuming a very fine lath width, PAG size and $M_{23}C_6$ diameter, which leads to significant over-prediction of initial yield stress and resultant cyclic behaviour, including failure, controlled by over-predicted softening. The microstructure prediction for PWHT ICHAZ and the resulting prediction of cyclic stress (Fig 15) is better than for AW ICHAZ. Hence, future work should focus on development of further improvements to modelling for the manufacturing-driven evolution of microstructure parameters. The recent work of Yang et al. [46, 47], on process-structure and structure-property prediction for laser-based powder bed fusion of Ti-6Al-4V alloy, shows an example of an improved approach.

5 Conclusions

This paper presents combined Gleeble physically-simulated welding and low cycle thermo-mechanical fatigue for P91 heat affected zone (HAZ), based on measured thermal histories from bead-on-plate welding trials. The welding physical simulation is designed to generate inter-critical HAZ material and to simulate post-weld treatment (PWHT). The inter-critical HAZ (ICHAZ) and parent material (PM) are subjected to in-phase (IP) and out-of-phase (OP) TMF testing, between 520 and 650 ^{o}C, to mimic possible severe thermal plant conditions, e.g. unintended “trip” conditions or future high temperature operation.

A key conclusion is that the PWHT-ICHAZ is found to be a weak region in TMF, compared to (i) as-welded (AW) ICHAZ for both IP and OP conditions and (ii) PM for IP conditions. For OP conditions, PWHT-ICHAZ gives similar performance to PM.

A recently-developed through-process, physically-based, thermal-metallurgical-mechanical model is adapted and applied to the simulated welding thermal cycle and TMF testing for PM and HAZ specimens, as well as to PM high temperature (isothermal) low cycle fatigue and TMF testing across different strain-ranges and strain-rates in the range 400^{o}C to 600^{o}C. For low cycle fatigue and TMF-IP and -OP conditions for PM up to 600^{o}C, the model is reasonably accurate with respect to cyclic stress and consistently conservative for life prediction. For TMF conditions up to 650^{o}C, the model gives similar level of agreement to tests for PM, both cyclic stress and life prediction; for ICHAZ, the model successfully captures the key trend of weak cyclic stress behaviour of PWHT, especially compared to AW. This is consistent with industry experience of the ICHAZ as a weak material region, e.g. Type IV cracking.

Further work is required to develop better relationships and understanding between physically-simulated welding and real welding processes and improved process-structure-property constitutive models and failure prediction models for complex TMF behaviour above 600^{o}C of welded 9Cr steels.

Acknowledgements

For the purpose of Open Access, the author has applied a CC BY public copyright licence to any Author Accepted Manuscript version arising from this submission. This research is funded by Science Foundation Ireland grant numbers SFI 22/FFP-A/10299 and supported in part by SFI/16/RC/3872. The authors would like to acknowledge the contributors to this research from

GE Power (UK), ESB Energy International, University of Limerick, Imperial College, London, and Fraunhofer IWM, Freiburg and IMDEA Madrid.

References

1. Ennis, P.J., Czyrska-Filemonowicz, A., *Recent Advances in Creep Resistant Steels for Power Plant Applications.* Operation Maintenance and Materials Issue, 2002. **1**(1).
2. Sauzay, M., Brillet, H., Monnet, I., Mottot, M., Barcelo, F., Fournier, B., Pineau, A., *Cyclically induced softening due to low-angle boundary annihilation in a martensitic steel.* Materials Science and Engineering A, 2005. **400-401**: p. 241-244.
3. Francis, J.A., Mazur, W., Bhadeshia, H. K. D. H., *Type IV cracking in ferritic power plant steels.* Materials Science and Technology, 2006. **22**(12): p. 1387-1395.
4. Farragher, T.P., Scully, S., O'Dowd, N. P., Hyde, C. J., Leen, S. B., *High Temperature, low cycle fatigue characterisation of P91 weld and heat affected zone material.* Journal of Pressure Vessel Technology, 2014. **136**: p. 021403-1 - 021403-10.
5. Shankar, V., Sandhya, R., Mathew, M.D., *Creep-fatigue-oxidation interaction in Grade 91 steel weld joints for high temperature applications.* Materials Science and Engineering A, 2011. **528**: p. 8428-8437.
6. Mac Ardghail, P., Harrison, N., Leen, S. B., *A process-structure-property model for welding of 9Cr power plant components: The influence of welding process temperatures on in-service cyclic plasticity response.* International Journal of Pressure Vessels and Piping, 2019. **173**: p. 26-44.
7. Bíró, T., Csizmadia, J., *Recent technique for thermal-fatigue simulation of heat-resistant steels.* Periodica Polytechnica, 2012. **56**: p. 105-110.
8. Castro Cerda, F., Goulas, C. Sabirov, I., Papaeftymiou, S., Monsalve, A., Petrov, R. H., *Microstructure, texture and mechanical properties in a low carbon steel after ultra fast heating.* Materials Science and Engineering A, 2016. **672**: p. 108-120.
9. Rahimian, M., Milenkovic, S., Maestro, L., De Azua, A. E. R., Sabirov, I., *Physical Simulation of Investment Casting of Complex Shape Parts.* Metallurgical and Materials Transactions A, 2015: p. 10.1007/s11661-015-2815-6.
10. DSI, *Thermal-Mechanical Simulators.* Gleeble Brochure, 2017.
11. Barrett, R.A. Experimental characterisation and computational constitutive modelling of high temperature degradation in 9Cr steel including microstructural effects, PhD Thesis, University of Galway, 2016
12. Sauzay, M., Brillet, H., Monnet, I., Mottot, M., Barcelo, F., Fournier, B., Pineau, A., Cyclically induced softening due to low-angle boundary annihilation in a martensitic steel. Materials Science and Engineering A, 2005. 400-401: p. 241-244.
13. Panait, C.G., Zielinska-Lipiec, A., Koziel, T., Czyrska-Filemonowicz, A., Gourgues-Lorenzon, A-F., Bendick, W.,, Evolution of dislocation density, size of subgrains and MX-type preipitates in a P91 steel during creep and during thermal ageing at 600oC for more than 100,000 h. Materials Science and Engineering A, 2010. 527: p. 4062-4069.
14. Ennis, P.J., Czyrska-Filemonowicz, A., Recent Advances in Creep Resistant Steels for Power Plant Applications. Operation Maintenance and Materials Issue, 2002. 1(1).
15. Barbadikar, D.R., Deshmukh, G. S., Maddi, L., Laha, K., Parameswaran, P., Ballal, A. R., Peshwe, D. R., Paretkar, R. K., Nandagopal, M., Mathew, M. D., Effect of normalizing and tempering temperatures on microstructure and mechanical properties of P92 steel. International Journal of Pressure Vessels and Piping, 2015. 132-133: p. 97-105.

16. Milovic, L., Vuherer, T., Blacic, I., Vrhovac, M., Stankovic, M., Microstructures and mechanical properties of creep resistant steel for application at elevated temperatures. Materials and Design, 2013. 46: p. 660-667.
17. Golden, B.J., Li, D-F., Guo, Y., Tiernan, P., Leen, S. B., O'Dowd, N. P., Microscale deformation of a tempered martensitic ferritic steel: Modelling and experimental study of grain and sub-grain interactions. Journal of Mechanics and Physics of Solids, 2016. 86: p. 42-52.
18. Farragher, T. Thermomechanical analysis of P91 power plant components, PhD Thesis, University of Galway, 2013
19. Yaghi, A.H., Hyde, T. H., Becker, A. A., Sun, W., Finite element simulation of residual stresses induced by the dissimilar welding of a P92 steel pipe with weld metal IN625. International Journal of Pressure Vessels and Piping, 2013. 111-112: p. 173-186.
20. Vallourec & Mannesmann Tubes, V & M Experience in T/P91 Tubes and Pipes, in International Workshop on Fabrication & Processing of Grade 91 Material, FAB 912011: Tiruchirappalli, India.
21. *ISO/TR 14745:2015(E).* The International Organisation for Standardisation, 2015.
22. S Scully, ESB Energy International, Personal Communication, April 2018.
23. Farragher, TP, O'Dowd, NP, Scully, S, Leen, SB, "Thermomechanical analysis of a pressurized plain pipe under realistic plant conditions," Trans ASME, J Pressure Vessel Technology, Feb 2013, vol 135, 011204, http://DOI:10.1115/1.4007287
24. Barrett, R.A., Hyde, C. J., O'Donoghue, P. E., Leen, S. B., *Thermomechanical fatigue in 9-12Cr steels: Life prediction models and the effect of tensile dwell periods.* International Journal of Fatigue, 2019. **126**: p. 335-245.
25. MacArdghail, P, Through-process Characterisation for Welding, Microstructure Evolution and Constitutive Response of 9Cr Steel Material for Flexible Power Plant Operation, PhD Thesis, University of Galway, 2020.
26. Li, M., Wang, L., Almer, J. D., Dislocation evolution during tensile deformation in ferritic-martensitic steels revealed by high-energy X-rays. Acta Materialia, 2014. 76: p. 381-393.
27. Nagesha, A., Valsan, M., Kannan, R., Bhanu Sanakara Rao, K., Mannan, S. L., Influence of temperature on the low cycle fatigue behaviour of a modified 9Cr-1Mo ferritic steel. International Journal of Fatigue, 2002. 24: p. 1283-1293.
28. Paul, V.T., Saroja, S., Hariharan, P., Rajadurai, A., Vijayalakshmi, M., *Identification of microstructural zones and thermal cycles in a weldment of modified 9Cr-1Mo steel.* Journal of Materials Science, 2007. **42**: p. 5700-5713.
29. Lojen G, Vuherer T. Optimization of PWHT of Simulated HAZ Subzones in P91 Steel with Respect to Hardness and Impact Toughness. Metals. 2020; 10(9):1215. https://doi.org/10.3390/met10091215.
30. Milovic, L.; Vuherer, T.; Blačić, I.; Vrhovac, M.; Stanković, M. Microstructures and mechanical properties of creep resistant steel for application at elevated temperatures. Mater. Design. 2013, 46, 660–667. https://doi.org/10.1016/j.matdes.2012.10.057
31. Marzocca, A.L.; Luppo, M.I.; Zalazar, M. Identification of precipitates in weldments performed in an ASTM A335 Gr P91 steel by the FCAW process. Procedia Mater. Sci. 2015, 8, 894–903. https://doi.org/10.1016/j.mspro.2015.04.150
32. Falat, L., Ciripová, L., Kepic, J., Bursik, J., Podstranká, I.,, *Correlation between microstructure and creep performance of martensitic/austenitic transition weldment in dependence of its post-weld heat treatment.* Engineering Failure Analysis, 2014. **40**: p. 141-152.
33. Li, D.-F., Barrett, R. A., O'Donoghue, P. E., Hyde, C. J., O'Dowd, N. P., Leen, S. B., *Micromechanical finite element modelling of thermo-mechanical fatigue for P91 steels.* International Journal of Fatigue, 2016. **87**: p. 192-202.
34. Zhao, L., Jing, H., Xu, L., Han, Y., Xiu, J., *Effect of residual stress on creep crack growth behaviour in ASME P92 steel.* Engineering Fracture Mechanics, 2013. **110**: p. 233-248.

35. Barrett, RA, O'Donoghue, P.E., Leen, SB, 'A physically-based constitutive model for high temperature microstructural degradation under cyclic deformation', Int J Fatigue, 100, 2017, 388-406. doi.org/10.1016/j.ijfatigue.2017.03.018
36. Shankar, V., Valsan, M., Bhanu Sankara Rao, K., Kannan, R., Mannan, S. L., Pathak, S. D., Low cycle fatigue behaviour and microstructural evolution of modified 9Cr-1Mo ferritic steel. Materials Science and Engineering A, 2006. 437: p. 413-422.
37. Abe, F., Tabuchi, M., Kondo, M., Tsukamoto, S., Suppression of Type IV fracture and improvement of creep strength of 9Cr steel welded joints by boron addition. International Journal of Pressure Vessels and Piping, 2007. 84: p. 44-52.
38. Basirat, M., Shrestha, T. Potirniche, G. P., Charit, I., Rink, K., *A study of creep behaviour of modified 9Cr-1Mo steel using continuum-damage modelling.* International Journal of Plasticity, 2012. **37**: p. 95-107.
39. Ó Murchú, C., Leen, S. B., O'Donoghue, P., Barrett, R. A., *A precipitate evolution-based continuum damage mechanics model of creep behaviour in welded 9Cr steel.* Journal of Materials Design and Applications, 2018.
40. Kintzel, O., Khan, S., Mosler, J., *A novel isotropic quasi-brittle damage model applied to LCF analyses of Al2024.* International Journal of Fatigue, 2010. **32**: p. 1948-1959.
41. Kumar, J., Singh, A. K., Ganesh Sundara Raman, S., Kumar, V., *Creep-fatigue damage modeling in Ti-6Al-4V alloy: A mechanistic approach.* International Journal of Fatigue, 2017. **98**(62-67).
42. Huffman, P.J., *A strain energy based damage model for fatigue crack initiation and growth.* International Journal of Fatigue, 2016. **88**: p. 197-204.
43. Rege, K., Pavlou, D. G., *A one-parameter nonlinear fatigue damage accumulation model.* International Journal of Fatigue, 2017. **98**: p. 234-246.
44. Lee, J.S., Maruyama, K., *Mechanism of Microstuctural Deterioration Preceding Type IV Failure in Weldment of Mod.9Cr-1Mo Steel.* Metallurgical Materials International, 2015. **21**: p. 639-645.
45. Zhou, J, Barrett, RA, Leen, SB, 'A physically-based method for predicting high temperature fatigue crack initiation in P91 welded steel', Int J Fatigue, 153, 2021, 106480. doi.org/10.1016/j.ijfatigue.2021.106480
46. Yang, X, Barrett, RA, Tong, M, Harrison, NM, Leen, SB, "Towards a process-structure model for Ti-6Al-4V during additive manufacturing" J Manufacturing Processes, 61, 2021, 428-439. doi.org/10.1016/j.jmapro.2020.11.033
47. Yang, X, Barrett, RA, Harrison, NM, Leen, SB, "A physically-based structure-property model for additively manufactured Ti-6Al-4V" Materials and Design, 205, 109709, 2021. 10.1016/j.matdes.2021.109709

Appendix 1 – High temperature low cycle fatigue test results for P91 material.

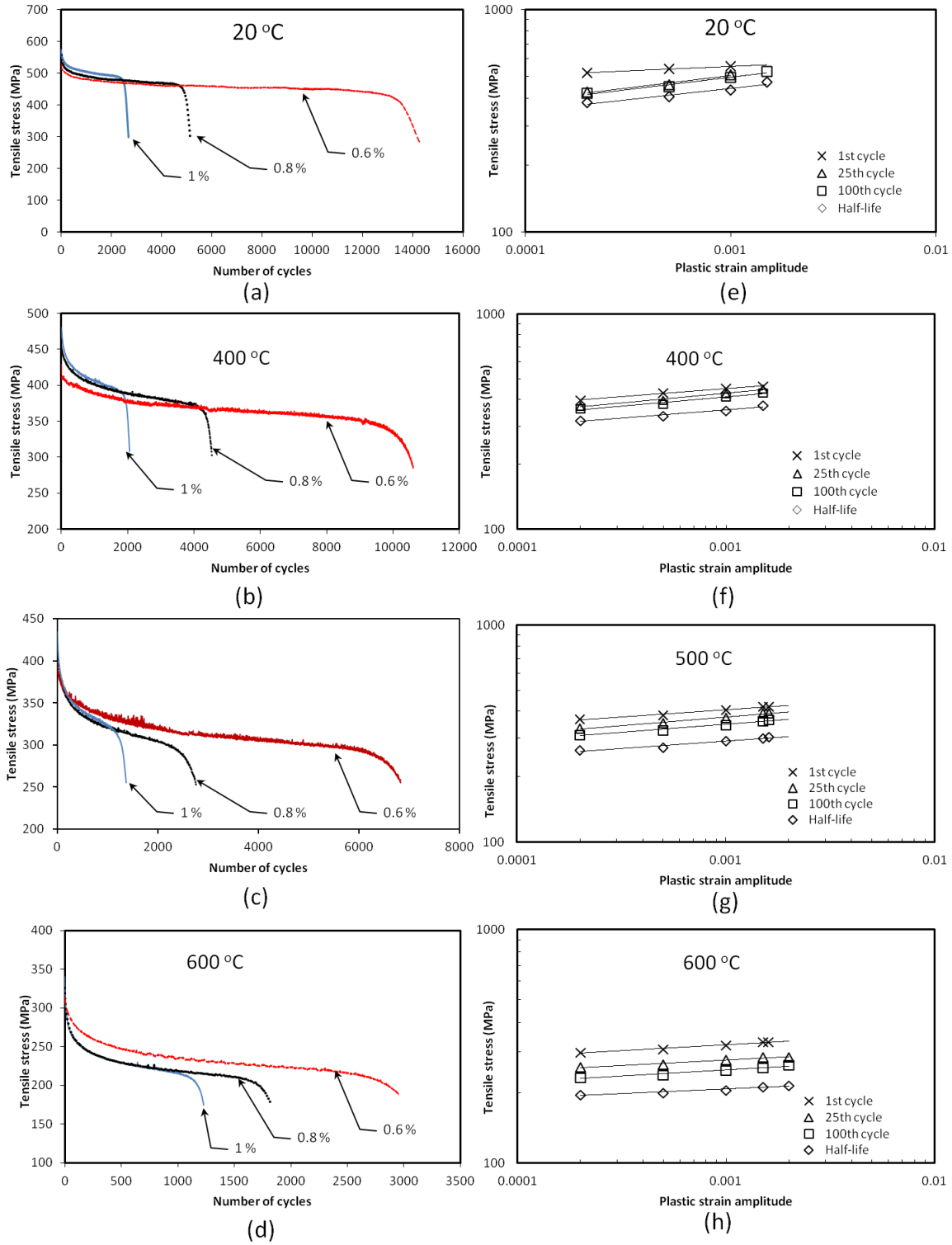

Figure A1.1 (a)–(d) Cyclic softening curves for P91 base material for a constant strain rate of 0.033 %/s at different temperatures. (e)–(h) Evaluation of stress-plastic strain power law relationship for various numbers of cycle for P91 base material at different temperatures [18].

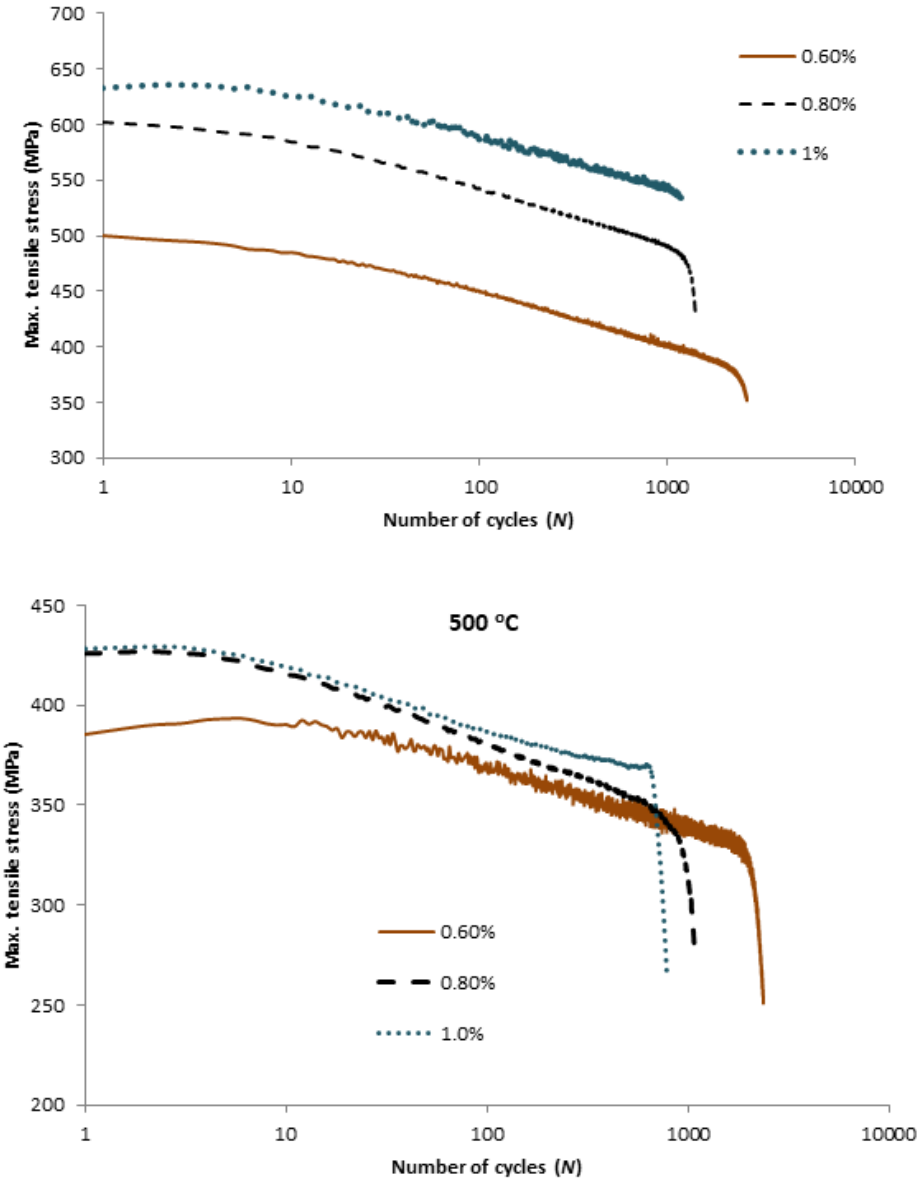

Figure A1.2. Sample HTLCF results for cross-weld P91 uniaxial specimens at 400 ^{o}C and 500 ^{o}C across a range of strain-ranges and for a strain-rate of 0.033 %/s [18].

Appendix 2

In this work, the parameters g_1 and $\bar{\rho}_L$ for martensite are defined by double-sigmoidal equations as a function of temperature, as follows:

$$g_1 = 0.5\left(J_p + J_s\right) + \frac{J_{r1}(T - J_{T1})0.5\left(J_p - J_s\right)}{\sqrt{1 + \left(J_{r1}(T - J_{T1})\right)^2}} + \frac{J_{r2}(T - J_{T2})0.5\left(J_f - J_p\right)}{\sqrt{1 + \left(J_{r2}(T - J_{T2})\right)^2}} + 0.5\left(J_f + J_p\right) \tag{A2.1}$$

$$\bar{\rho}_L = 0.5\left(P_p + P_s\right) + \frac{P_{r1}(T - P_{T1})0.5\left(P_p - P_s\right)}{\sqrt{1 + \left(P_{r1}(T - P_{T1})\right)^2}} + \frac{P_{r2}(T - P_{T2})0.5\left(P_f - P_p\right)}{\sqrt{1 + \left(P_{r2}(T - P_{T2})\right)^2}} + 0.5\left(P_f + P_p\right) \tag{A2.2}$$

The seven parameters controlling the rate-term, g_1, are constants (Table A2.1). It was found that the parameters P_p, P_s, P_f, P_{r1} and P_{r2} are dependent on the lath width whereas P_{T1} and P_{T2} are not (Table A1).

In the austenite phase, g_1 (Eqn. 15) is defined by a linear equation:

$$g_1 = g_2 + g_3 T \tag{A2.3}$$

and $\bar{\rho}_L$ (austenite phase) is defined by:

$$\bar{\rho}_L = 0.5\left(P_p^\gamma + P_s^\gamma\right) + \frac{P_{r1}^\gamma\left(T - P_{T1}^\gamma\right)0.5\left(P_p^\gamma - P_s^\gamma\right)}{\sqrt{1 + \left(P_{r1}^\gamma\left(T - P_{T1}^\gamma\right)\right)^2}} \tag{A2.4}$$

The model parameters for Eqns. A2.3 and A2.4 are shown in Table A2.1.

Table A2.1. Identified parameters for the dislocation-density evolution model [25].

Parameter	Value
J_p	383
J_s	55
J_f	90
J_{r1}	0.015 K^{-1}
J_{r2}	0.05 K^{-1}
J_{T1}	550 ^oC
J_{T2}	720 ^oC
P_p	$0.867 - 0.014(\mathrm{nm}^{-0.5})\sqrt{L}$
P_s	$0.27 - 0.0024(\mathrm{nm}^{-0.5})\sqrt{L}$
P_f	$0.0976 - 0.0009(\mathrm{nm}^{-0.5})\sqrt{L}$

P_{r1}	$-0.0077 + 0.0015(\mathrm{nm}^{-0.5})\sqrt{L}$
P_{r2}	$0.0225 + 0.0003(\mathrm{nm}^{-0.5})\sqrt{L}$
P_{T1}	275 ^{o}C
P_{T2}	555 ^{o}C
g_2	6.443
g_3	0.0225 K^{-1}
P_p^{γ}	0.3
P_s^{γ}	0.9
P_{r1}^{γ}	0.01 K^{-1}
P_{T1}^{γ}	710 ^{o}C

Note: *L* is dislocation mean path length.